



Cite this: *Nanoscale*, 2015, **7**, 4306

Rational design of two-dimensional molecular donor–acceptor nanostructure arrays

Jia Lin Zhang,^{†[a,b](#)} Shu Zhong,^{†[b](#)} Jian Qiang Zhong,^{a,b} Tian Chao Niu,^b Wen Ping Hu,^c Andrew Thye Shen Wee^a and Wei Chen^{*[a,b,d,e](#)}

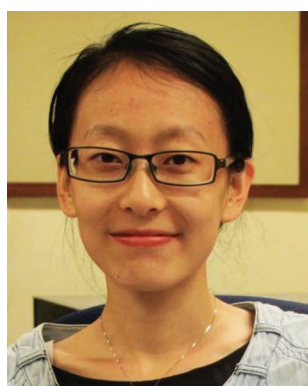
The construction of long-range ordered organic donor–acceptor nanostructure arrays over microscopic areas supported on solid substrates is one of the most challenging tasks towards the realization of molecular nanodevices. They can also be used as ideal model systems to understand light induced charge transfer, charge separation and energy conversion processes and mechanisms at the nanometer scale. The aim of this paper is to highlight recent advances and progress in this topic. Special attention is given to two different strategies for the construction of organic donor–acceptor nanostructure arrays, namely (i) molecular self-assembly on artificially patterned or pre-defined molecular surface nanotemplates and (ii) molecular nanostructure formation steered *via* directional and selective intermolecular interactions. The interfacial charge transfer and the energy level alignment of these donor–acceptor nanostructures are also discussed.

Received 14th November 2014,
Accepted 2nd February 2015

DOI: 10.1039/c4nr06741j
www.rsc.org/nanoscale

1. Introduction

Electronic devices based on organic semiconductors (conjugated organic small molecules or polymers) are considered as a promising alternative to their inorganic counterparts, offering the possibility of producing large area, low cost, flexible, lightweight and multifunctional devices.¹ Significant advancement has been made in the fields of organic light-emitting diodes (OLEDs),^{2–5} organic photovoltaics (OPVs)^{6–12} and organic field effect transistors (OFETs),^{13–18} and a number of applications have been demonstrated. OLEDs, developed for



Jia Lin Zhang

Jialin Zhang received her Bachelor's degree in Physics from Sichuan University in 2010 and PhD degree from Physics Department at National University of Singapore (NUS) in 2014. She is currently a postdoctoral research fellow in the Chemistry Department at NUS. Her research interests include molecular self-assembly, single molecule manipulation and two-dimensional material growth.



Wei Chen

Dr Chen Wei is currently an Associate Professor in both Chemistry Department and Physics Department at National University of Singapore (NUS). He received his Bachelor's degree in Chemistry from Nanjing University (China) in 2001 and a Ph.D. degree from the Chemistry Department at NUS in 2004. His current research interests include molecular-scale interface engineering for molecular, organic and graphene electronics, and interface-controlled nanocatalysis for energy and environmental research.

application in flat panel displays and solid state lighting, are now available as commercial products such as car stereos, cell phones, camcorders and radios.¹⁹ OPVs, owing to their flexibility and light weight, are suited to applications as chargers for portable electronic devices or as a ‘smart fabric’ for integrating into various textiles and fabrics.²⁰ The rapid development of OFETs makes them promising candidates for application in sensors, displays, smart cards, radio-frequency identification tags as well as in integrated circuits.¹⁹

A common feature of most organic electronic devices is that they are composed of multilayer stacking structures.^{21–24} Multiple metal-organic, organic-organic, and organic-inorganic interfaces are created from this multilayered device configuration. In OLED, the introduction of the hole transport layer (HTL), the electron transport layer (ETL) in addition to the emitter layer (EL) allows controlling and optimizing the charge injection, charge transport and recombination in OLED.²¹ A similar multilayer stacking strategy has also been used in OPVs, which can facilitate the charge separation, charge transport and charge collection.²² In ambipolar OFETs, the laminated or interpenetrated organic heterojunctions are used as p-type and n-type conducting channels, which represent an effective approach to fabricating organic integrated circuits.²³

The organic-organic heterojunctions created from thin films of two different organic semiconductor materials are essential components in the organic electronic device. For example, in a typical OPV multilayer architecture, efficient exciton dissociation and charge separation occurs at the donor-acceptor (D-A) interfaces.^{25–28} The D-A heterojunctions are formed by the donor material with a low ionization potential (IP) and the acceptor material with a high electron affinity (EA). The variation of electron and hole potentials across this interface is strong and favors exciton dissociation. OPVs can adopt either planar heterojunction or bulk heterojunction formats by laminating, blending, co-deposition or chemical linking of the donor and acceptor materials.^{25–27} However, since the exciton diffusion length (L_D) is typically an order of magnitude smaller than the optical absorption length (L_A), in the planar D-A heterojunction a large fraction of the photo-generated excitons are formed beyond the diffusion length of the interface. So, the exciton will decay through luminescence instead of contributing to the photocurrent. An alternative approach to overcoming the exciton diffusion bottleneck is to form a bulk heterojunction (BHJ). As shown in Fig. 1, bulk heterojunctions are characterized by an interpenetrating network of donor and acceptor materials, providing a large interface area where the dissociation of excitons into separated electrons and holes can efficiently occur. In this case, all excitons are created within the diffusion length of a D-A interface. If continuous pathways exist in each material from the interface to the respective electrodes, the power conversion efficiency will be greatly enhanced. The energy level diagram of a model organic solar cell is also shown in Fig. 1. There are four steps for the generation of the photocurrent: (1) absorption of an incident photon to create an exciton; (2) diffusion of the exciton to the donor-acceptor interface; (3) exciton dis-

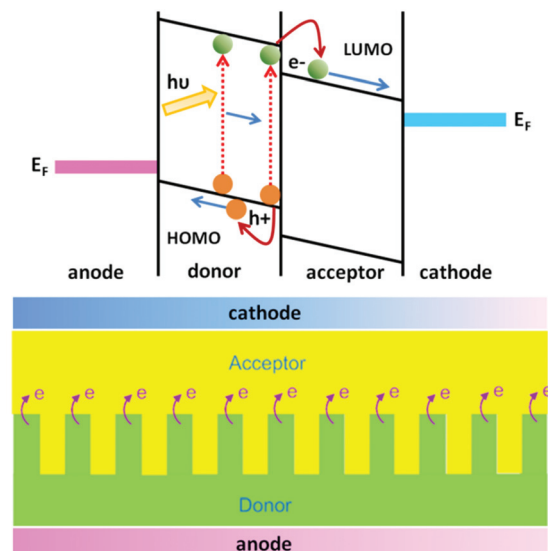


Fig. 1 The schematic drawing of energy diagrams of organic solar cells and the relevant donor–acceptor interface constructed from a well-ordered molecular donor–acceptor nanostructure array, which has a large interface area for exciton dissociation.

sociation at the donor-acceptor interface and transfer of the electron to the acceptor or the hole to the donor for excitations in the donor or acceptor layers, respectively; (4) charge transport of the photo-generated electron and hole to the cathode and anode, respectively.^{7,29}

The interface properties of the D-A heterojunction are of fundamental importance for the device performance. The particularly important factors for device operation are the interface nanostructuring and energy level alignment.^{19,30} Much effort has been devoted to engineer the D-A interface, for example, manipulation of the supramolecular packing and molecular orientation to maximize the interface area as well as to achieve higher charge carrier mobility; controlling the energy-level offsets between the LUMO of the acceptor molecules and HOMO of the donor molecules to maximize the open circuit voltage (V_{oc}) and hence the power conversion efficiency.^{31,32}

To better control the organic nanostructure formation and energy level alignment to improve the power conversion efficiency of the device, it is highly desirable to investigate the donor-acceptor system at the molecular scale. This requires the rational design of well-defined molecular donor-acceptor nanostructure arrays. Supramolecular self-assembly represents a promising approach to construct long-range ordered organic donor-acceptor nanostructure arrays over macroscopic areas supported on solid substrates. By selecting the molecular building blocks with desired functionalities and structures, the highly ordered nanostructure arrays can be used as model systems for gaining a comprehensive understanding of the film morphology, charge transfer and charge separation processes at the interfaces.

In this review article, we highlight recent advances in the fabrication of two-dimensional (2D) molecular donor-acceptor

nanostructure arrays through two different approaches, (i) molecular self-assembly on artificially patterned or pre-defined molecular surface nanotemplates, and (ii) multicomponent 2D assemblies steered *via* multiple intermolecular interactions. In combination with *in situ* photoelectron spectroscopy studies, the interfacial charge transfer and the energy level alignment for these model donor–acceptor systems are discussed.

2 Molecular self-assembly on artificially patterned or pre-defined molecular surface nanotemplates

2.1 Formation of surface nanotemplates by molecular self-assembly

One of the central challenges in nanotechnology is the development of highly adaptable methodologies for creating well defined molecular architectures at surfaces. The utilization of supramolecular chemistry offers promise in this regard. The basic concept of supramolecular chemistry is rooted in the exploration of molecular recognition events that take advantage of spontaneous and reversible non-covalent interactions for the assembly of either a few or many components into well organized nanostructures.³³ Selective non-covalent interactions, including hydrogen bonding,^{34–38} metal–ligand coordination,^{39,40} van der Waals,^{41,42} and dipole–dipole interactions,^{43,44} have been widely exploited both in solution and in the solid state to prepare extended assemblies. By selecting molecular building blocks with desired functionalities and structures, a rich variety of molecular architectures have been realized, such as isolated clusters,⁴⁴ one-dimensional (1D) supramolecular chains or nanogratings,³⁷ 2D extended networks^{34,39,41} as well as more complex multicomponent arrangements.^{45,46} Some of the resulting molecular nanostructures are appealing because they provide preferential binding sites. These molecular monolayers can be used as nanostructured templates for building more complicated hierarchical structures, thus expanding the capabilities of bottom up nanotechnology *via* self-assembly. By rational design and selection of molecular building blocks, the surface nanotemplates can be tailored to porous or non-porous organic,³⁴ metal–organic³⁹ and inorganic⁴⁷ networks with different nanocavity sizes or periodicities. The aggregation patterns of the template form honeycomb,³⁴ rectangular,³⁹ kagome, nanomesh^{47,48} or nanostripe arrays^{49–51} by tuning the non-covalent interactions between individual adsorbed molecules.

Elegant examples of surface nanotemplates include the 2D open honeycomb networks stabilized by triple hydrogen bonding between melamine and perylene tetra-carboxylic di-imide (PTCDI) on Ag-passivated Si(111) substrates;³⁴ and 2D rectangular metal–organic coordination networks (MOCNs) comprising tailored pore size and chemical functionality by modular assembly of polytopic organic carboxylate linker molecules and iron atoms on the Cu(100) surface.³⁹ The relatively stronger hydrogen bonds or coordination bonds usually

lead to more rigid networks. The van der Waals interaction based on alkyl-chain interdigititation can be employed to create a flexible host network, as demonstrated by conformational changes of the dehydrobenzo annulene (DBA) molecular network in response to addition of guest coronene molecules.⁴¹

2.2 Construction of molecular donor–acceptor nanostructure arrays using surface nanotemplates

Various versatile extended templates with programmable shape, size, functionality and bonded by single component, binary or even multi-component subunits have been prepared on the surface.⁵² An important application of these 2D pre-patterned surface nanotemplates is to selectively accommodate guest molecules inside the nano-cavities or to couple functional molecules at the preferential adsorption sites.^{53–56} In particular, the regularity of the network offers the possibility of fabricating the organic donor–acceptor nanojunction arrays in a repetitive and spatially ordered arrangement.

In many high efficiency OPVs, C₆₀ has been chosen to serve as an acceptor material. This is due to the many advantageous properties of C₆₀ arising from its spherical symmetry: (1) the intersystem crossing resulting from large orbital angular momentum inherent in the π-electron system converts all excited states to triplets with correspondingly long diffusion lengths; (2) it can pack tightly to form highly conductive films with excellent orbital overlap between adjacent molecules, thereby improving both the electron and exciton diffusion efficiency.²⁷ In this section, we demonstrate the construction of various organic donor–acceptor nanostructure arrays using the molecular templates and C₆₀ molecules as donor and acceptor materials respectively.

2.2.1 Donor–acceptor nanostructure arrays formed by C₆₀/oligothiophene on graphite. A surface with a well-defined periodicity can serve as a molecular template and provide binding sites, and is a bottom-up route for the fabrication of highly ordered arrays of guest molecules. As shown in Fig. 2a₁,⁵⁷ oligothiophene 1 self-assembles on highly oriented pyrolytic graphite (HOPG) into a long-range network made of two types of elongated cavities having different sizes and shapes. Post-deposition of C₆₀ leads to the formation of defect-free alignment of C₆₀ molecules by site-selective inclusion into the largest extremity of the horizontal cavities, as indicated in the schematic of Fig. 2a₂. With compound 1 and C₆₀ being electron-donating and accepting molecules respectively, this model system may be useful for the future development of photovoltaic devices.

Shape-persistent macrocycles, which are composed of a rigid molecular backbone and flexible side groups, can be used as promising building blocks to serve as a template for self-assembly.⁵⁸ Fig. 2b₁ shows a high-resolution STM image of ordered arrays of macrocycle 2 on HOPG under ambient conditions. The macrocycles are organized into rows and separated by alkyl chains. These chains are interdigitated and orientated along one of the main symmetry axes of the underlying HOPG to maximize their interaction with the substrate.

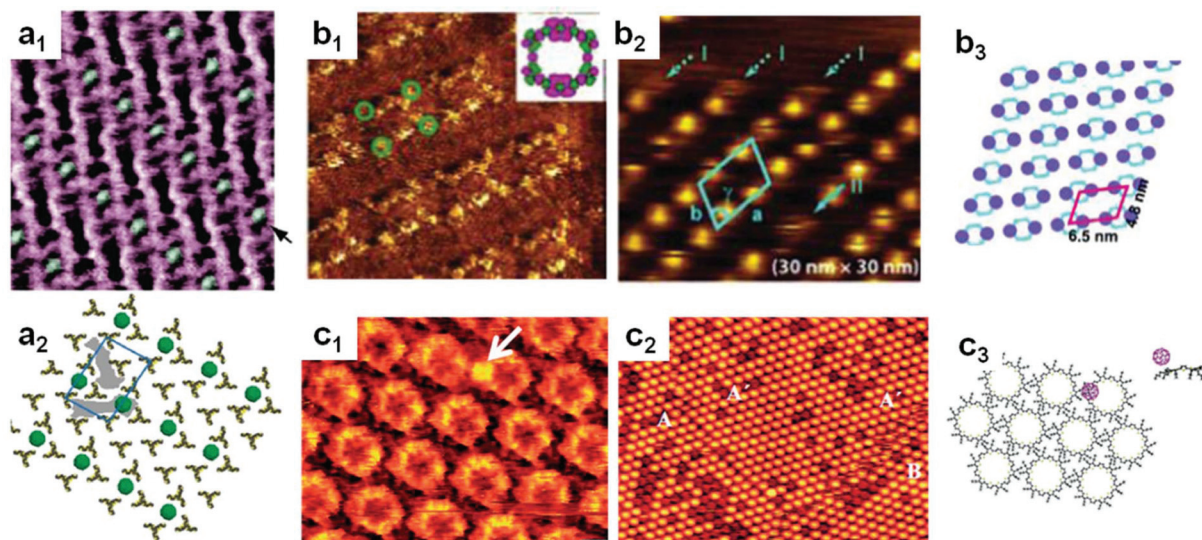


Fig. 2 Construction of molecular donor–acceptor nanostructure arrays by using molecular surface nanotemplates. (a) STM images of a star-shaped oligothiophene 1–C₆₀ guest–host network on graphite, $21 \times 21 \text{ nm}^2$, $V_s = 0.3 \text{ V}$, $I = 40 \text{ pA}$. Individual C₆₀ molecules appear in green and are indicated by an arrow (top), a model of the long-range alignment of single C₆₀ in the open network of 1 (bottom). The STM image is obtained at room temperature. (b) High-resolution STM image of ordered arrays of the shape consistent macrocycle 2 on HOPG under ambient conditions, $V = 0.41 \text{ V}$, $I = 0.5 \text{ nA}$, the four extra-angular groups are indicated with green circles, the inset is the HOMO of the cyclic backbone of 2 (b1), ordered arrays of 2/C₆₀ on HOPG under ambient conditions, $V = 1.0 \text{ V}$, $I = 0.3 \text{ nA}$, arrows I and II indicate individual macrocycles (b2), the proposed structural model showing that the C₆₀ molecules are located at the two sides of the macrocycle (b3). The STM images are obtained at room temperature. (c) STM image of a monolayer of cyclo[12]thiophene (C[12]T) on HOPG, including a C[12]T–C₆₀ complex (white arrow), image area: $11.6 \times 8.7 \text{ nm}^2$, $V = -700 \text{ mV}$, $I = 44 \text{ pA}$ (c1), C[12]T–C₆₀ complexes at higher C₆₀ coverage (c2), the calculated model of a closely packed monolayer of C[12]T with a hexagonal arrangement, the upper right corner is the side view of the calculated energy minimum conformation of a C[12]T–C₆₀ complex (c3). The STM images are obtained at room temperature. (a) Reprinted from ref. 57, with permission from the American Chemical Society, copyright 2009; (b) reprinted from ref. 58, with permission from the American Chemical Society, copyright 2006; (c) reprinted from ref. 59, with permission from the Wiley-VCH Verlag GmbH & Co. KGaA, copyright 2006.

Co-deposition with C₆₀ leads to the formation of fullerene–oligothiophene composites, where the C₆₀ molecules are located at the two sides of the macrocycle (Fig. 2b₂ and 2b₃). This clearly shows that the driving force for this superstructure is the donor–acceptor interaction between C₆₀ and the electron rich units of the ring. The prepared 2D supramolecular structures can be further used as a template for complex 3D structures.

Another example of the fullerene–oligothiophene composites is the complexation of C₆₀ on a cyclo[12]thiophene (C[12]T) monolayer template.⁵⁹ Fig. 2c₁ shows a representative STM image of a well ordered cyclothiophene monolayer on HOPG. Semiempirical calculations on the macrocycles indicate that the energetically most-favorable geometry is a “spider-like” conformation with an almost planar π-system (Fig. 2c₃). The alkyl side chains bend out of the thiophene plane to allow for intermolecular interactions between the alkyl side chains of adjacent molecules. Upon adsorption of C₆₀ on top of this modified template surface, C₆₀ molecules form a stable 1:1 donor–acceptor complex with the electron-rich cyclothiophene. Semiempirical calculations corroborate that the most stable complexation site is at the rim of the macrocycle, providing maximal π–π interactions, as shown in the schematic of Fig. 2c₃. At high coverage, the complexed C₆₀ forms a 2D hexagonal structure, with cell parameters well matched with the underlying macrocycle monolayer, as shown in Fig. 2c₂. The

above results demonstrate that self-assembled highly ordered oligothiophenes on graphite can be used as veritable templates to steer the formation of donor–acceptor nanoarchitectures with C₆₀ fullerenes.

2.2.2 Donor-acceptor nanostructure arrays formed by C₆₀/6T on Ag(111). As mentioned above, self-assembly of donor–acceptor arrays using the rigid templates is demonstrated, where the host molecules are structurally persistent during the guest molecule addition. The donor–acceptor arrays can also be constructed using a “soft” molecular template. In these cases, a complete monolayer of host molecules on the surface is still required for the successful formation of the donor–acceptor structures. These host molecules on the surface can help reduce the interaction between the guest molecule and the underlying surface; however, in contrast to the rigid template, during the donor–acceptor structure formation process, the host molecule itself undergoes dynamic structural rearrangement, thereby referred to as a “soft” molecular template. In this section, we describe the formation of tunable C₆₀ arrays on the α-sexithiophene (6T) molecular surface nanotemplate on Ag(111) by carefully tuning the molecular ratio of C₆₀:6T and the post-annealing temperature.^{49,50} Room temperature (RT) deposition of 1 monolayer (ML) 6T on Ag(111) results in the formation of highly periodic 6T nanostripes. As shown in Fig. 3a, the rod-like feature represents a

single 6T molecule. They adopt a side-by-side packing with the molecular plane oriented parallel to the surface.⁴⁵ Further deposition of 0.5 ML C₆₀ molecules on the 6T nanostripes results in the random arrangements of C₆₀. Post-annealing the sample at 380 K for 10 min leads to the formation of highly ordered C₆₀ molecular-chain arrays with an interchain distance of 2.31 nm (Fig. 3b). The distance between the two neighboring chains is shorter than the lateral periodicity of 6T nanostripes (2.74 nm). It is proposed that the intermolecular interaction between C₆₀ and 6T could induce structural rearrangement of 6T during annealing. Fig. 3c shows the proposed structural model for the C₆₀ single-chain arrays. If we start with a substrate covered with 1.5 ML 6T (Fig. 3d), tunable C₆₀ linear chains can be fabricated by varying the intermolecular ratio, the post-annealing temperature and the annealing time.⁴⁷ Again, RT deposition of 0.1 ML C₆₀ on bilayer 6T does not lead to any ordered arrangement of C₆₀ molecules. After annealing the sample at 360 K for 30 min, unique C₆₀ dot arrays dominate the surface, as shown in the high-resolution STM image of Fig. 3e. Post-annealing at the same temperature (360 K) for a longer time can result in the transformation from C₆₀ dot arrays to C₆₀ rail-like chains (Fig. 3f). Further increasing the C₆₀ coverage to 0.35 ML and annealing at 360 K for another 30 min leads to the appearance of C₆₀ pair-like chains, as shown in Fig. 3g. Unlike the short-range ordering of C₆₀ rail-like chains or C₆₀ dot chains, the well-ordered C₆₀ pair-like chain arrays can extend to several hundreds of nanometers.

The fabrication of a regular donor–acceptor nanostructure array by self-assembly relies on a rational choice of both (1) the complementary building blocks for intermolecular interactions and (2) an appropriate surface to guide the long-range growth of the supramolecular nanostructures. It is well known that binary molecular systems usually undergo phase separation or form randomly mixed domains.⁶⁰ However, in the C₆₀/6T system, the formation of well ordered C₆₀ chain arrays is accompanied by the rearrangement of underlying 6T molecules. The intermolecular interaction is expected to be dominated by the donor–acceptor interaction between 6T and C₆₀. During the experiment, three different domains of C₆₀ molecule chain arrays rotated by 60° with respect to each other have been observed, reflecting the symmetry of the Ag(111) substrate. In addition, these C₆₀ superstructures only appear after deposition of C₆₀ on a 6T monolayer or a bilayer, whereas the adsorption of C₆₀ on submonolayer 6T results in the formation of two separate domains of hcp C₆₀ and poorly ordered 6T. All these results demonstrate that the Ag(111) substrate plays a key role in the formation of C₆₀ chain arrays. This idea can be further confirmed by assembling C₆₀ on 6T monolayer nano-stripes on graphite.^{61,62} In this case, the molecule–substrate interfacial interactions are dominated by π–π interactions compared with the strong coupling between the 6T electrons and Ag d-band electrons. As shown in Fig. 4, RT deposition of C₆₀ on a 6T monolayer on HOPG results in the formation of random C₆₀ networks comprising three elementary structural

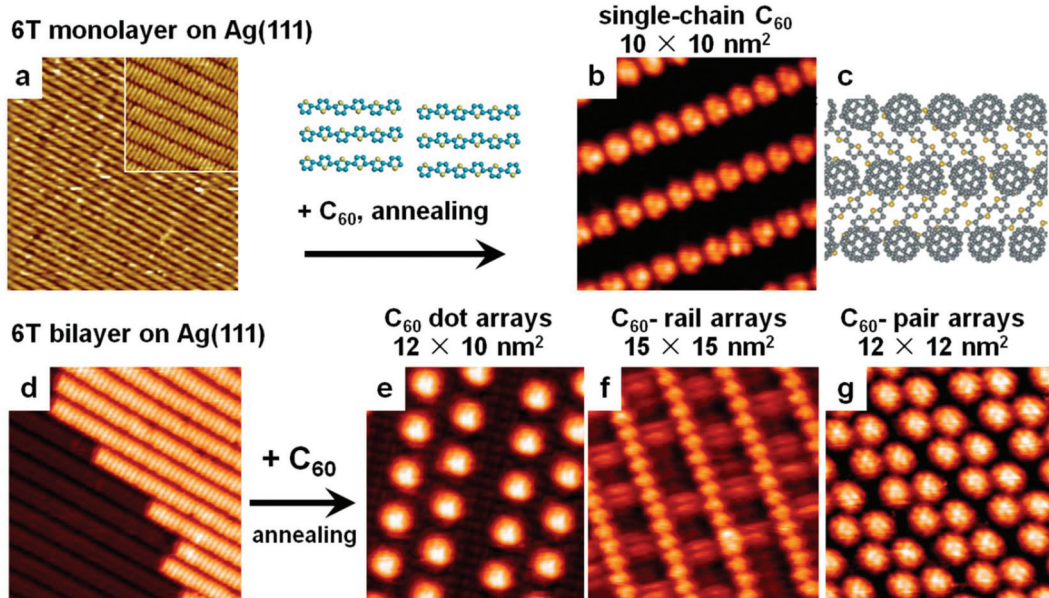


Fig. 3 (a) STM image of the long-range-ordered 6T nanostripes formed by annealing the Ag(111) covered with 1 ML RT-deposited 6T at 400 K; a high-resolution view of the molecular structure of 6T nanostripes is shown in the inset ($V_{\text{tip}} = -1.70$ V, $I = 150$ pA, $T = 77$ K). (b) High-resolution STM image (10×10 nm²) of the perfectly ordered C₆₀ single-chain arrays formed by further depositing 0.6 ML C₆₀ on the 6T nanostripes and subsequent annealing at 380 K ($V_{\text{tip}} = -1.80$ V, $I = 70$ pA, $T = 77$ K). (c) The proposed structural model of C₆₀ single-chain arrays. (d) STM image of the 6T bilayer consisting of 1.5 ML 6T molecules on Ag(111). (e) High-resolution STM image (12×10 nm²) of the C₆₀ dot arrays ($V_{\text{tip}} = -1.40$ V, $I = 70$ pA, $T = 77$ K). (f) High-resolution STM image (15×15 nm²) indicating that the rail-like molecule arrays consist of continuous C₆₀ linear chains and interlinked 6T molecules ($V_{\text{tip}} = -1.44$ V, $I = 70$ pA, $T = 77$ K). (g) High-resolution STM image (12×12 nm²) revealing the detailed structure of the C₆₀-pair chain arrays ($V_{\text{tip}} = -1.6$ V, $I = 100$ pA, $T = 77$ K). (a) Reprinted from ref. 49, with permission from the Wiley-VCH Verlag GmbH & Co. KGaA, copyright 2007; (b–g) reprinted from ref. 50, with permission from the Wiley-VCH Verlag GmbH & Co. KGaA, copyright 2008.

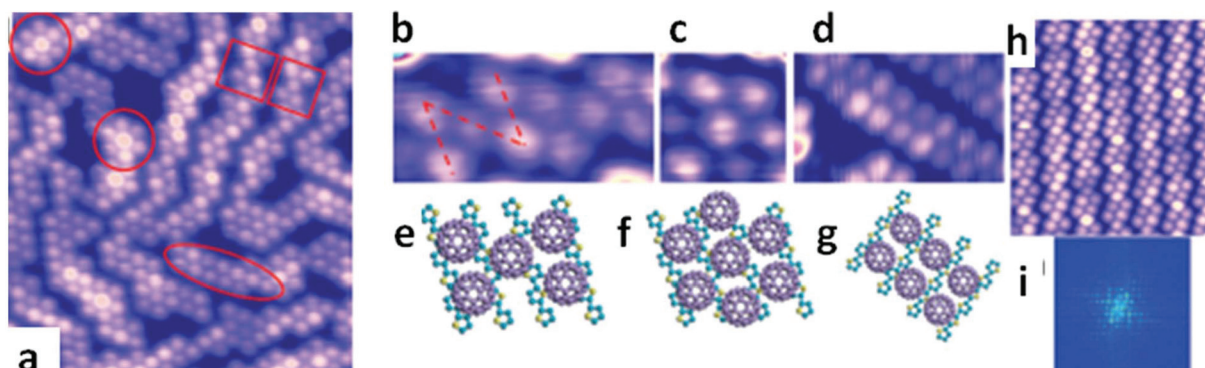


Fig. 4 (a) STM image of 0.5 ML C_{60} on 6T on HOPG, $20 \times 20 \text{ nm}^2$ ($V_{\text{tip}} = -1.9 \text{ V}$, $T = 77 \text{ K}$); the rectangles, circles and ellipse highlight the three elementary structural motifs of the zigzag filament, hexagon and C_{60} -pair filament, respectively. (b–d) Moleculary resolved STM image of the identified three elementary structural motifs: (b) the zigzag filament, (c) the hexagon and (d) the C_{60} -pair filament, and the corresponding schematic models (e–g) are attached below each panel. (h) $20 \times 20 \text{ nm}^2$ STM image of the ordered zigzag C_{60} chain arrays on HOPG ($V_{\text{tip}} = -2.2 \text{ V}$, $T = 77 \text{ K}$) after annealing at 350 K and its corresponding FFT image is shown in (i). (a–i) Reprinted from ref. 62, with permission from the American Institute of Physics, copyright 2011.

motifs: a C_{60} zigzag filament, a C_{60} hexagon and a C_{60} -pair filament. Further annealing the binary system at elevated temperature can increase molecular surface mobility and allow them to transform into the most stable C_{60} zigzag motif. As a result, highly ordered “zigzag” C_{60} chain arrays form on the 6T monolayer nanostripes on graphite. Hence, the formation of the tunable, long-ranged ordered C_{60} chain arrays on 6T nanostripes on Ag(111) is proposed to arise from the delicate balance between the homo-intermolecular (C_{60} - C_{60} and

6T-6T, van der Waals), hetero-intermolecular (C_{60} -6T, donor-acceptor interaction) and molecule–substrate interactions (π -d interaction for 6T-Ag).^{61,62}

2.2.3 Donor-acceptor nanostructure arrays formed by C_{60} /6P on Ag(111). In this section, we demonstrate the construction of donor–acceptor nanojunction arrays by adsorbing C_{60} on the surface nanotemplate of *p*-sexiphenyl (6P) nanostripes on Ag(111).⁵¹ Fig. 5a shows the STM image of well ordered unidirectional 6P nanostripes fabricated by RT deposition of 1 ML

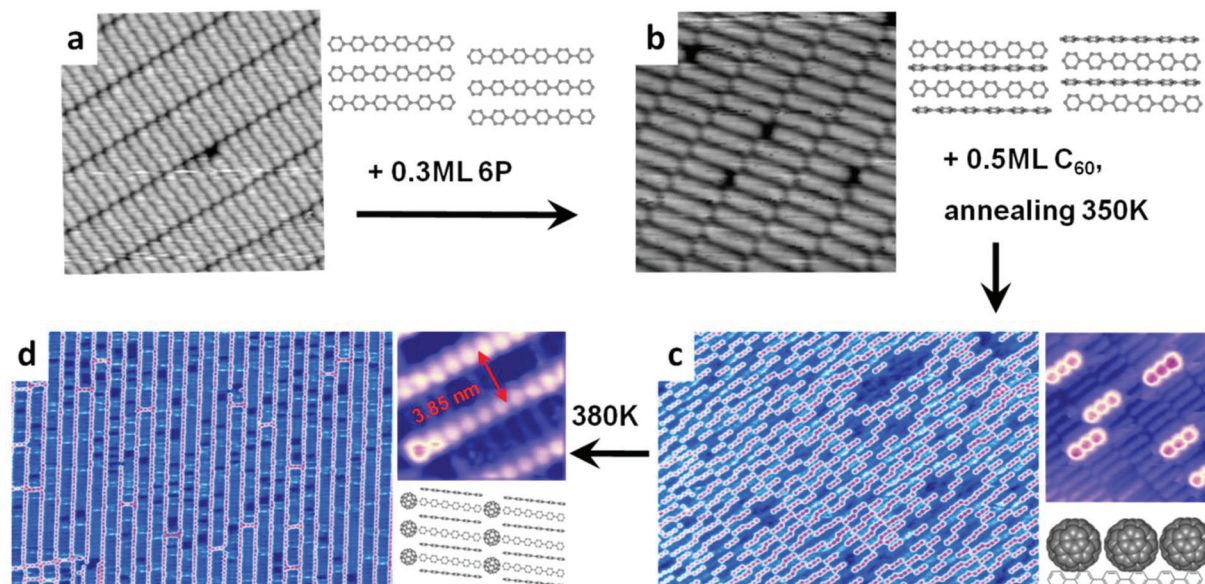


Fig. 5 (a) $15 \times 15 \text{ nm}^2$ STM images of “pure face-on” ($V_{\text{tip}} = 1.8 \text{ V}$, $T = 77 \text{ K}$) and (b) “face-on + edge-on” ($V_{\text{tip}} = -3.3 \text{ V}$, $T = 77 \text{ K}$) 6P monolayer nanostripe on Ag(111); the corresponding schematic drawings of the molecular structure for both 6P nanostripes are shown on the right. (c) STM image ($V_{\text{tip}} = 1.4 \text{ V}$, $T = 77 \text{ K}$) of C_{60} triplet arrays or vertical C_{60} /6P nanojunction arrays formed after the deposition of 0.5 ML C_{60} on “face-on + edge-on” 6P layers followed by annealing at 350 K (left); the corresponding detailed $15 \times 15 \text{ nm}^2$ STM image ($V_{\text{tip}} = 1.4 \text{ V}$, $T = 77 \text{ K}$), showing the preferential trapping of every three C_{60} molecules on a single 6P molecule and the proposed molecular model (right). (d) STM image ($V_{\text{tip}} = -2.0 \text{ V}$, $T = 77 \text{ K}$) of lateral C_{60} /6P nanojunction arrays formed after annealing the C_{60} triplet array at 380 K (left); the corresponding detailed STM image ($V_{\text{tip}} = -2.0 \text{ V}$, $T = 77 \text{ K}$) and the proposed molecular model for the regular superlattice of alternating C_{60} and 6P linear chains. (a–d) Reprinted from ref. 51, with permission from the American Institute of Physics, copyright 2008.

6P on Ag(111) and subsequent annealing at 380 K for 30 min. Each rod-like feature represents a single 6P molecule. The formation of 6P monolayer nanostripes on Ag(111) can be understood in terms of self-assembly *via* side-by-side packing with extended molecular π -plane parallel to the Ag(111) surface. This structure is referred to as the “pure face-on” 6P nanostripes. Further deposition of 0.3 ML 6P molecules can result in the insertion of edge-on 6P molecules into the matrix of the pure face-on 6P nanostripes, where the edge-on represents the configuration of 6P molecules with all their phenyl rings oriented nearly perpendicular to the substrate surface. As shown in the schematic of Fig. 5b, this leads to the alternating arrangement of face-on and edge-on 6P nanostripe arrays with larger periodicity, referred to as “face-on + edge-on” 6P nanostripes.

RT adsorption of 0.5 ML C₆₀ on the “face-on + edge-on” 6P nanostripes, and subsequent annealing at 350 K for 30 min, leads to a fairly ordered 2D C₆₀ triplets array (Fig. 5c). The corresponding high-resolution STM image and the schematic model in Fig. 5c reveal a unique preferential trapping of the C₆₀ triplet atop a single 6P molecule. These C₆₀ triplets assemble along the underlying 6P nanostripe packing direction and are proposed to predominantly nucleate on the edge-on 6P molecules.

Annealing the C₆₀/6P vertical nanojunction array at 380 K for 30 min can result in the transformation of a C₆₀ triplet array into a highly periodic C₆₀ linear chain array, as shown in Fig. 5d. The interchain distance was measured to be 3.85 nm, which is close to the sum of van der Waals radii of C₆₀ and the molecule length of 6P. As such, we propose a model involving the insertion of C₆₀ linear chains into the “face-on + edge-on” 6P nanostripes arrays. Such lateral organic donor/acceptor nanojunction arrays may find potential applications in organic solar cells. We have also investigated C₆₀ on 6P monolayer covered HOPG. In this system, we cannot observe any visible intermixing or nanoscale phase separation. A molecularly sharp C₆₀/6P interface with hexagonally-close-packed C₆₀ layers on a 6P layer has been revealed.⁶³

3 Molecular nanostructure formation *via* the directional, selective intermolecular interactions

3.1 Various molecular architectures sustained through multiple intermolecular interactions

Molecular assemblies of increasing complexity can also be spontaneously formed based on multiple intermolecular interactions. Self-assembly of 2D supramolecular structures by intermixing molecular species with complementary functional groups represents another promising approach for construction of a complex donor–acceptor system. These binary or multi-component supramolecular arrays are sustained through intermolecular interactions, such as directional and selective hydrogen bonding,^{34–36,64} metal–ligand coordination,⁴⁰ less

specific van der Waals forces,⁴⁶ or strong covalent bonding.^{65,66}

By carefully selecting molecular building blocks with desired functionality, geometry as well as an appropriate molecule ratio, the resulting supramolecular architectures can be tailored to a rich variety of patterns. Elegant examples include the intermixed PTCDI-melamine phase with chirality on Au(111) stabilized by triple hydrogen bonding between PTCDI and melamine (Fig. 6a);⁶⁴ “double-row” metal–organic coordination networks formed by modular assembly of trimellitic acid molecules and iron atoms on the Cu(100) substrate, as shown in Fig. 6b;⁴⁰ a complex four-component architecture of bisDBA-C12, coronene (COR), isophthalic acid (ISA) and triphenylene (TRI) at the solid–liquid interface of HOPG based on van der Waals interactions (Fig. 6c);⁴⁶ the construction of 2D covalent bonded networks on Au(111) by controlling the position of active end groups in bromophenyl porphyrin Br_xTPP, as illustrated in Fig. 6d.⁶⁶

3.2 Hydrogen-bonded tunable donor–acceptor nanostructure arrays on graphite

Most of the surface supported assemblies based on weak van der Waals interactions bear the disadvantage of low thermal and mechanical stability. The construction of covalent bonded networks through polymerization reactions of deposited molecules shows higher stability, but they are more difficult to control. Directional and selective hydrogen bonds, which are of intermediate strength relative to the weak van der Waals force and strong covalent bonding, represent the most versatile and widely employed means of directing the organization of molecular building blocks into supramolecular systems with appreciable stability and tunability.

Tunable intermixed donor–acceptor nanostructure arrays can be constructed by exploiting multiple intermolecular hydrogen bonding.^{38,67–70} This is demonstrated using binary combinations of molecules with different geometries, namely, copper hexadecafluorophthalocyanine (F₁₆CuPc) with *p*-sexiphenyl (6P), pentacene or di-indenoperylene (DIP) on HOPG.⁴⁵ Fig. 7a shows the first binary system of F₁₆CuPc embedded in a 6P molecular matrix with an intermolecular ratio of 1 : 1. The long rod-like feature represents a single 6P molecule and the four-lobe feature represents an F₁₆CuPc molecule. Both F₁₆CuPc and 6P molecules lie flat on HOPG with their conjugated π -plane parallel to the substrate. Two F₁₆CuPc are inter-linked by a single 6P molecule, forming an oblique F₁₆CuPc dot array with the unit cell of $c_1 = 1.60$ nm, $d_1 = 2.99$ nm, and $\alpha_1 = 96^\circ$. Intermixing F₁₆CuPc with pentacene at the same intermolecular ratio results in the formation of a new packing structure. As shown in Fig. 7b, the bright shot rod-like feature represents a single pentacene molecule, and the unit cell is tuned to $c_2 = 1.84$ nm, $d_2 = 1.86$ nm, $\alpha_2 = 79^\circ$. The tunability of self-assembled molecular nanostructures is further demonstrated by the third binary system of F₁₆CuPc with DIP, which has an elliptical shape. As shown in Fig. 7c, the bright leaf-like feature represents a single DIP molecule and the unit cell of this F₁₆CuPc dot array is $c_3 = 1.91$ nm, $d_3 = 1.91$ nm, $\alpha_3 = 77^\circ$.

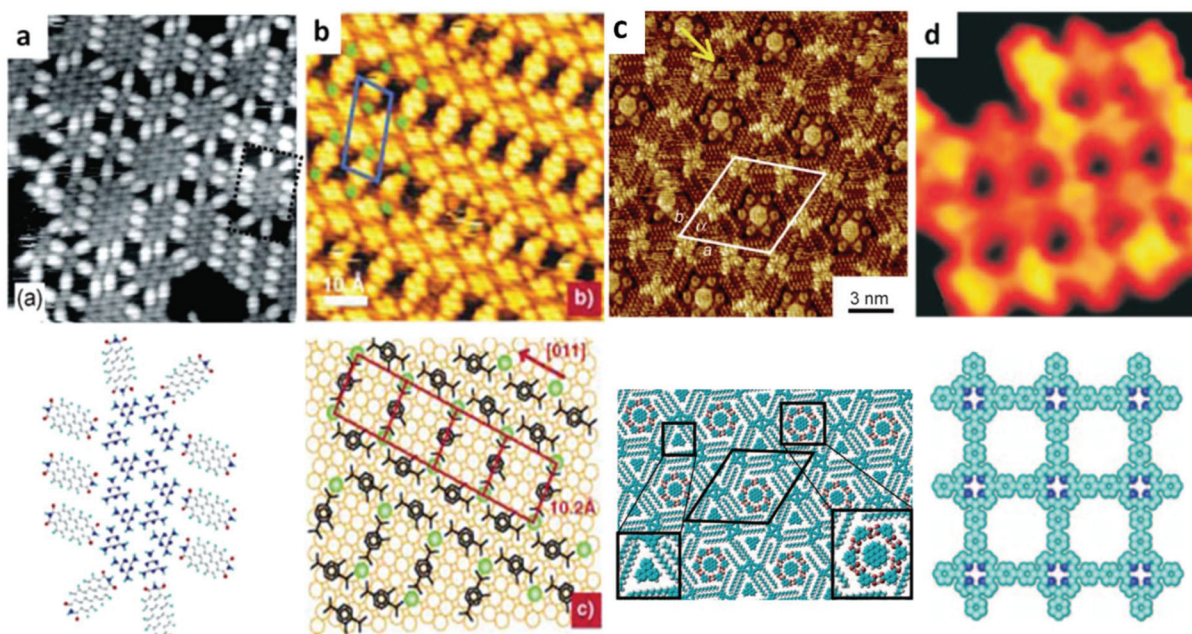


Fig. 6 Various molecular nanostructures formed on surfaces steered via the directional, selective non-covalent or covalent intermolecular interactions. (a) Intermixed PTCDI–melamine phase formed after annealing the sample adsorbed with PTCDI and melamine at 50 °C, $19.7 \times 19.7 \text{ nm}^2$, $V = -1.8 \text{ V}$, $I = 0.05 \text{ nA}$; the figure shows melamine islands around which PTCDI molecules are attached through hydrogen bonding (top); schematic of the PTCDI attachment to the melamine array – this corresponds to the region marked by dotted lines in part a (bottom). The STM image is obtained at room temperature. (b) High-resolution STM image of a “double-row MOCN” assembled by tuning the coverage ratio to one Fe atom per tmla molecule, single protrusions at the points of intersection throughout the network are associated with Fe atoms, laterally coordinated by tmla carboxylate moieties, the unit cell of the network is marked in blue and Fe atoms around are colored green (top), a tentative model for the double-row Fe-carboxylate MOCN, the side carboxylate groups are assumed to be oriented perpendicular to the surface, Fe atoms are arranged in a ladder-type structure with a $1.02 \times 1.02 \text{ nm}^2$ repeat unit (bottom). The STM image is obtained at room temperature. (c) STM image of a mixture of bisDBA-C12, COR, ISA, and TRI, $V = 1.10 \text{ V}$, $I = 0.053 \text{ nA}$ (top), a tentative network model showing the Kagome structure of bisDBA-C12 hosting the COR1-ISA6 cluster and TRI in the hexagonal and triangular voids, respectively (bottom). The STM image is obtained at room temperature. (d) Nano-architectures of covalently bound Br_4TPP molecular networks (top) and the corresponding chemical structures of the nanostructures (bottom), $T = 7 \text{ K}$. (a) Reproduced from ref. 64, with permission from American Chemical Society, copyright 2006; (b) reproduced from ref. 40, with permission from Wiley-VCH Verlag GmbH & Co. KGaA, copyright 2003; (c) reproduced from ref. 46, with permission from Wiley-VCH Verlag GmbH & Co. KGaA, copyright 2009; (d) reproduced from ref. 66, with permission from Nature Publishing Group, copyright 2007.

The corresponding simulated molecular superstructures are given below each STM image and the possible intermolecular C–F…C–H hydrogen bonds are highlighted. To better understand the structural stability of these binary systems, density functional theory (DFT) calculations are performed to evaluate the total intermolecular binding energy. It reveals that the structural stability of these 2D binary molecular networks is sustained through the formation of multiple intermolecular C–F…C–H hydrogen bonds between the electronegative periphery F atom of F_{16}CuPc and the electropositive periphery H atom of 6P, pentacene, or DIP.⁴⁵

3.3 Charge-transfer donor–acceptor complexes on metallic surfaces

For the donor–acceptor heterojunction adsorbed on the metallic substrate, the intermolecular interactions can be affected by the hybridization and screening at the metallic interface. The adsorption induced charge transfer, structural distortions and hybridization with metal states can cause the realignment, splitting and broadening of the original molecular states.^{71–73} Gonzalez-Lakunza *et al.* demonstrated this effect by using the

monolayer of a charge-transfer complex tetrathiafulvalene-tetracyanoquinodimethane (TTF-TCNQ) on the Au(111) surface as an example.⁷² The TTF-TCNQ molecular solid bulk phase has only a fractional charge transfer of 0.6 electron from the donor π stacks (TTF) to the acceptor ones (TCNQ). However, on the Au(111) surface the TTF-TCNQ complex has different stacking geometries and charge transfer magnitudes. As shown in Fig. 8a and its corresponding high-resolution image in Fig. 8c, TTF and TCNQ molecules self-assemble into 1:1 mixed domains comprising alternating rows of donor and acceptor species with their molecular π plane parallel to the Au(111) surface. Excess TCNQ molecules can segregate into pure islands. DFT calculations using the model in Fig. 8d reveal that a molecular layer is bonded to the Au(111) through TTF *via* two S–Au bonds,⁷⁴ while the TCNQ molecules only interact weakly with the metal surface. Fig. 8e shows the differential conductance (dI/dV) spectra recorded on a pure TCNQ island and the clean Au(111) surface. SS indicates the Au(111) surface states. An LUMO resonance at 0.7 V can be observed on a pure TCNQ island. However, for the same spectrum recorded on the mixed island on a TCNQ molecule (Fig. 8f), the peak at 0.7 V

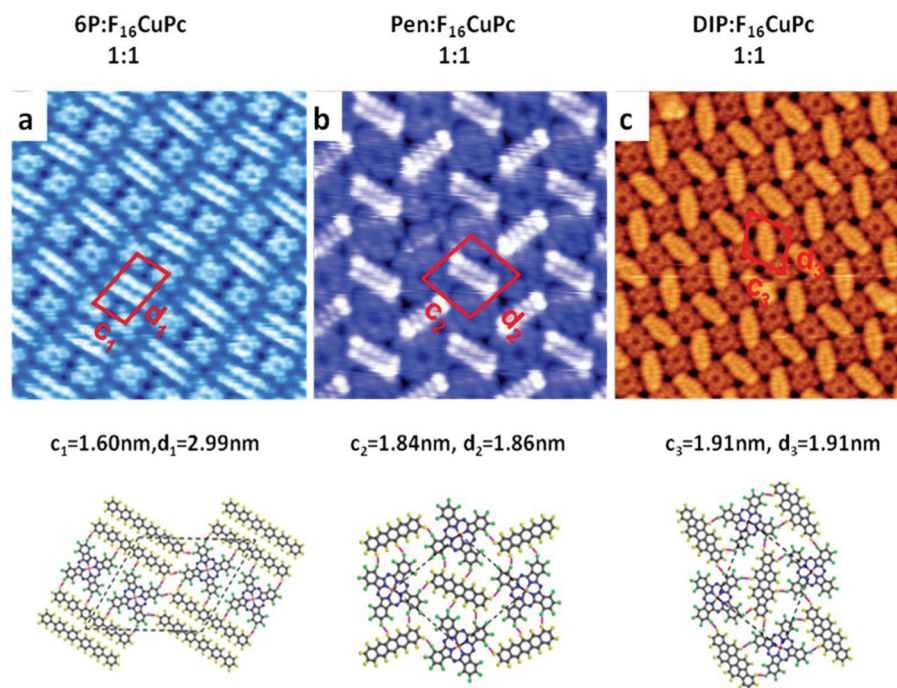


Fig. 7 Molecular resolved STM images of F_{16}CuPc molecular dot arrays with tunable intermolecular distance controlled by the geometrical parameters of the co-adsorption molecules. (a) $6\text{P} : \text{F}_{16}\text{CuPc} = 1 : 1$ ($V_{\text{tip}} = 2.0$ V, $15 \times 15 \text{ nm}^2$, $T = 77$ K). (b) $\text{Pen} : \text{F}_{16}\text{CuPc} = 1 : 1$ ($V_{\text{tip}} = 2.5$ V, $10 \times 10 \text{ nm}^2$, $T = 77$ K). (c) $\text{DIP} : \text{F}_{16}\text{CuPc} = 1 : 1$ ($V_{\text{tip}} = 2.0$ V, $15 \times 15 \text{ nm}^2$, $T = 77$ K). The DFT simulated molecular models are shown below each STM image. (a–c) Reprinted from ref. 45, with permission from the Wiley-VCH Verlag GmbH & Co. KGaA, copyright 2010.

disappears, while a sharp peak (IS1) at 0.3 V emerges. At the same time, the surface state SS is no longer observed in this mixed phase. These results suggest that TTF-TCNQ layer modifies the electronic structure of the Au(111) surface and causes additional features to appear in the LUMO region.

DFT calculations were carried out to unravel the origin of these newly emerged molecular states.⁷² Fig. 8g shows the projecting density of states (PDOS) for TTF and TCNQ molecules in both mixed phase and the free molecular chains. It is found that the PDOS of the TCNQ molecule keep their line shape upon adsorption, in agreement with its weak interaction with the surface. However, a downshift of the molecular orbital aligns its LUMO with E_F , and hence the TCNQ molecule becomes singly occupied. For the TTF molecule, its HOMO suffers a large broadening due to its mixing with the surface states, becoming partially unoccupied. This further confirms that the interaction of the mixed layer with the Au(111) surface is essentially conducted by the TTF molecule. The single occupation of the TCNQ LUMO is further verified by its vibrational Kondo effect, which is due to the localization of an unpaired electron in the conjugated LUMO.⁷⁵ This localization is due to sufficient decoupling of the TCNQ molecule from the underlying metal surface by lateral interaction with the TTF molecules. The above results demonstrate that on the metal surfaces, the charge transfer between the donor and the acceptor is not simply governed by the IP and EA. Effects such as hybridization with the substrate and charge screening must also be included.

4. Application of the donor–acceptor heterojunction as a molecular rectifier

The rectifier is an important component in electronic devices that allows the current to flow in one direction but blocks it in the opposite direction. Molecular rectifiers were first suggested by Aviram and Ratner, where a single molecule comprising a donor and an acceptor unit separated by a sigma bonded tunneling bridge is expected to show rectifying properties.⁷⁶ The underlying mechanism of this effect is based on the energy level alignment of the HOMO of the donor and the LUMO of the acceptor. During the past few decades, the most widely suggested and experimentally tested candidates for rectifiers are a single molecule compound that has an electron donor and an electron acceptor moiety chemically linked by a sigma bond.^{77–83} Apart from single molecule rectifiers, the junctions formed by two different self-assembled monolayers (SAM) on two metal electrodes brought into contact^{84,85} or the donor–acceptor heterojunctions formed *via* a layer-by-layer electrostatic adsorption also exhibit a rectifying effect.^{86,87} Bera *et al.* have demonstrated a molecular rectifier based on the NiPc/PB donor–acceptor heterojunctions formed on highly doped Si(111) (PB represents copper hexacyanoferrate, which is an analogue of Prussian Blue).⁸⁸ Current–voltage (I – V) characteristics of the molecular junctions were measured with a STM tip under ambient conditions. As shown in Fig. 9a, the NiPc/PB

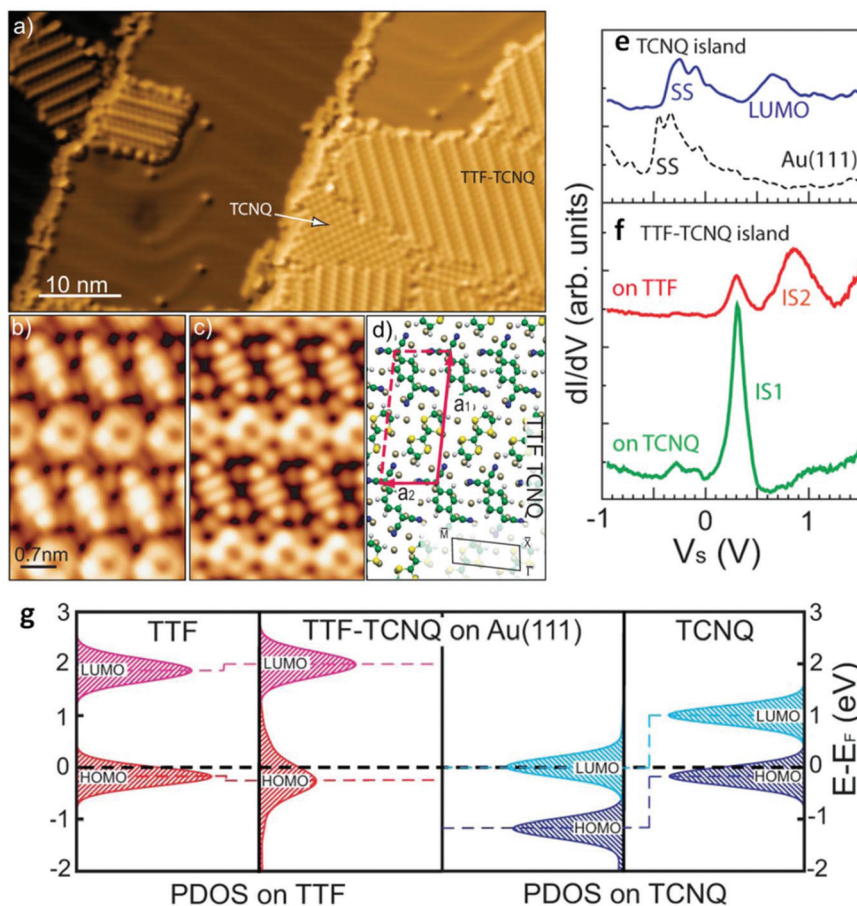


Fig. 8 TTF-TCNQ charge transfer complex on the Au(111) surface. (a) STM image of TTF-TCNQ domains on Au(111). Excess TCNQ molecules appear to be segregated in pure islands ($V_s = 1.7$ V, $I_t = 0.1$ nA, $T = 5$ K). (b) Intramolecular structure of TTF and TCNQ resembling the shape of the HOMO and LUMO, respectively ($V_s = 0.3$ V, $I_t = 0.4$ nA, $T = 5$ K). (c) Simulated constant current STM image ($V_s = 1.0$ V, $T = 5$ K) using the Teroff–Hamann approach on the DFT minimized structure shown in (d). (e) Comparison of differential conductance spectra of TCNQ pure islands [spectrum taken on a nearby clean Au(111) region shown for comparison] and (f) TTF and TCNQ in mixed TTF-TCNQ islands. (g) DOS of the TTF-TCNQ/Au(111) system projected on TTF and TCNQ orbitals around E_F , compared with the PDOS of free molecular chains of each component. (a–g) Reprinted from ref. 72, with permission from American Physical Society, copyright 2008.

(D/A) assembly shows a larger current at a negative tip voltage, while the PB/NiPc (A/D) assembly shows a larger current at a positive tip voltage. Since NiPc and PB act as the donor and the acceptor of the heterojunction, respectively, a negative tip voltage is a forward-bias for the D/A assembly, while a positive tip voltage is forward-bias for the A/D assembly. However, the rectification ratio is not impressive (highest ratio being 1.8 at 2.5 V). This ratio can be enlarged by orienting the magnetic moments of the donor and acceptor layers in the same direction. Fig. 9c shows the I - V curves for the NiPc(\uparrow)/PB(\uparrow) and PB(\uparrow)/NiPc(\uparrow) assemblies, where the rectification ratio is increased to 3.7 and 2.6 at 2.5 V, respectively. The same I - V curves measured for the NiPc(\downarrow)/PB(\downarrow) and PB(\downarrow)/NiPc(\downarrow) assemblies show ratios of 3.2 and 2.7 at 2.5 V, respectively. With the magnetic moments of the donor and acceptor layers being parallel to each other, the electron transfer through the junction becomes spin-polarized and hence more efficient, resulting in an increased rectification.

5. Charge transfer and the energy level alignment at these donor–acceptor nanostructure interfaces

To better utilize the donor–acceptor nanostructures in various applications, it is essential to fully understand the nature of the interactions at the donor–acceptor heterojunction interfaces, as well as the interfacial energy level alignment. It is believed that possible π – π interactions, hydrogen bonding, dipole–dipole interaction and the weak donor–acceptor interaction play a key role in the formation of organic nanostructures. Photoelectron spectroscopy (PES) (including ultraviolet photoelectron spectroscopy (UPS) and X-ray photoelectron spectroscopy (XPS)) is a powerful method to examine the degree of charge transfer or the strength of the donor–acceptor interactions, as well as the interfacial energy level alignment.^{31,89}

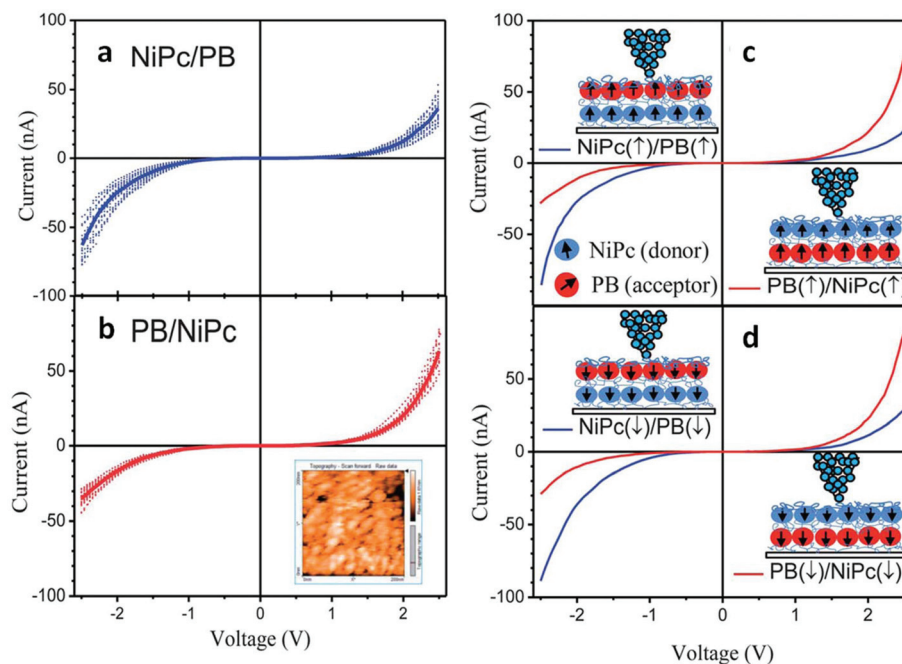


Fig. 9 Current–voltage characteristics of (a) NiPc/PB and PB/NiPc assemblies recorded at 20 different points each. The thick lines in each of the two plots are averages of the characteristics. STM topography of a PB/NiPc assembly is shown in the inset. (c) and (d) Current–voltage characteristics of NiPc/PB and PB/NiPc assemblies with moments of the components parallel and both facing outwards (up/up) and downwards (down/down). The insets of the figures show a schematic presentation of the respective moments in the D/A and A/D assemblies. (a–d) Reprinted from ref. 88, with permission from Royal Society of Chemistry, copyright 2013.

5.1 Charge transfer and energy level alignment in monolayer donor–acceptor blends

5.1.1 Donor–acceptor monolayer blends formed by Pen- $F_{16}CuPc$ on Au(111). In addition to the intensive studies on the structural properties of donor–acceptor nanostructures, enormous research effort has also been devoted to their electronic properties. Formation of the donor–acceptor monolayer blends on a surface provides a perfect platform to study both the intermolecular and molecule–substrate interfacial interactions, as interfaces between the neighboring molecules and molecule–substrate are simultaneously formed in this system.^{89–94} Oteyza *et al.* have demonstrated the universal core-level shift as a function of the molecular donor/acceptor ratio.⁹⁰ Fig. 10a shows the C 1s core-level spectra of the Pen- $F_{16}CuPc$ system on Au(111) at different donor–acceptor stoichiometries. As the concentration of donor molecules (Pen) decreases from the pure donor monolayer, through donor–acceptor blends, to the pure acceptor ($F_{16}CuPc$) monolayer, a shift of the C 1s core level to lower binding energy is observed. The same trend is also observed for the valence band region (Fig. 10b). As shown in Fig. 10c, a core-level shift of the donor–acceptor blends can also be reproduced by the DFT calculation of a free-standing Pen- $F_{16}CuPc$ system. The good match between the experimental shift and DFT calculations of the free-standing layer indicates that Pen- $F_{16}CuPc$ interacts weakly with Au(111). A comparison of the measured and calculated core-level shifts, HOMO shifts and work function shifts for both Pen and $F_{16}CuPc$ is plotted in Fig. 10d. The

shift of these molecular levels by the same amount suggests a rigid donor–acceptor band structure. Usually, the “oxidation” (“reduction”) of donor (acceptor) molecules shifts core levels to higher (lower) binding energy. However, in this system, the sign of the shift is at odds with the charge flow direction. This is because the core-level shift is a combination effect of the charge transfer and the change in the effective potential. In this system, minor oxidation/reduction effects are compensated for and even reversed by the effective potential created by their neighboring molecules. Fig. 10e shows a schematic diagram of the energy-level alignment at the pure donor, pure acceptor layers and the donor–acceptor blends on metal surfaces. The changes of the vacuum level rigidly shift all molecular levels (core level and valence band) by the same amount. They have also measured the electronic structures for other donor–acceptor interfaces (Pen- $F_{16}CuPc$ on Au(111), Ag(111), Cu(111) and CuPc-PFP on Au(111), Ag(111) and Cu(111)) and observe the same trend for the core-level shift. Such a core-level tracking method can be used to determine the charge carrier injection/extraction barrier.

5.1.2 Donor–acceptor monolayer blends formed by CuPc- $F_{16}CuPc$ on HOPG. For some of the donor–acceptor nanostructures prepared on metal surfaces, the strong coupling between the molecule and the substrate may induce the interface hybrid electronic states. This will complicate the understanding of the intrinsic donor–acceptor intermolecular interactions. The inert graphite can serve as an ideal substrate for the probing of the intrinsic molecular electronic states, for

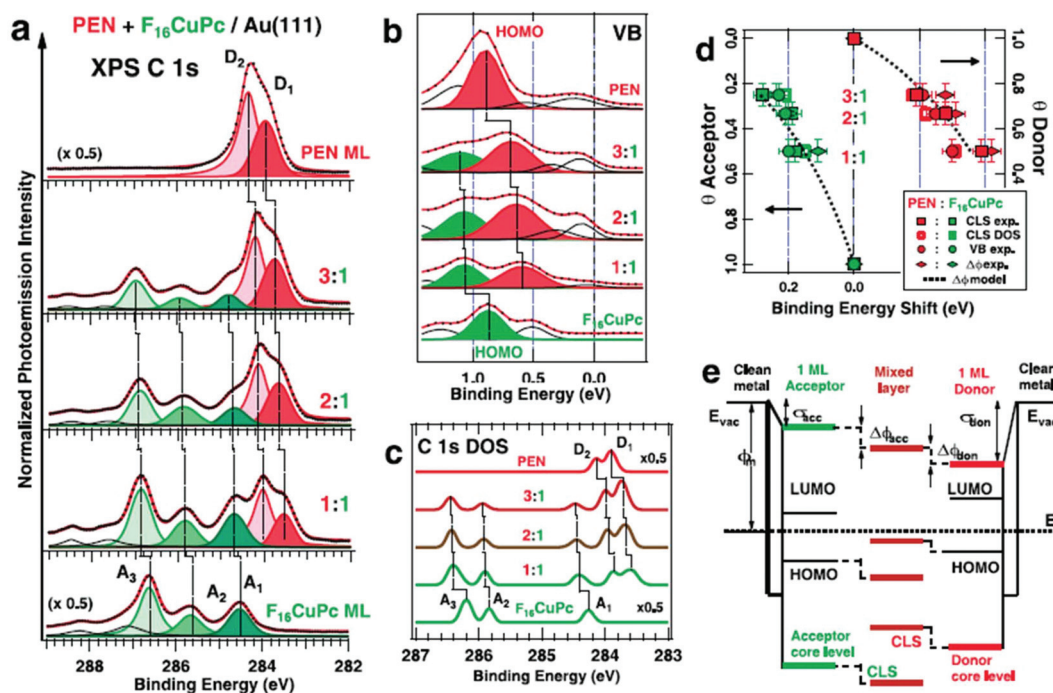


Fig. 10 (a) C 1s core-level spectra and (b) valence band spectra from donor-rich (top) to acceptor-rich (bottom) monolayer blends, measured by photoemission on the Pen-F₁₆CuPc/Au(111) system. HOMO levels are identified from the comparison with thick film spectra. Features above the HOMO level and up to E_F vanish in thick films and hence are assumed as interface hybrids. (c) C 1s core levels for Pen-F₁₆CuPc/Au(111) of varying concentration calculated by DFT for free-standing monolayers. (d) Calculated and measured A₁ and D₁ core-level shifts for Pen-F₁₆CuPc/Au(111) interfaces. The HOMO peaks and changes in work function for varying stoichiometry are shown by circles and diamonds. The dotted line corresponds to the estimated work function change using pure donor and acceptor layers. All core-level, HOMO, and vacuum-level shifts take the reference from pure donor or acceptor layers and show comparable results. (e) Schematic diagram of the energy-level alignment of single-component layers and donor–acceptor blends on metal surfaces. The varying vacuum levels and the associated shift of molecular levels upon donor–acceptor blend formation in a vacuum-level pinning scenario are highlighted by dotted lines. Reprinted from ref. 90, with permission from American Chemical Society, copyright 2013.

example, the energy level alignment in the weakly interacting CuPc-F₁₆CuPc donor–acceptor system on graphite.⁸⁹ Fig. 11a shows the UPS spectra at the low binding energy region for a CuPc and F₁₆CuPc monolayer and their 1 : 1 mixture on HOPG. It is observed that by forming the CuPc-F₁₆CuPc binary structure, the HOMO peaks for CuPc and F₁₆CuPc are shifted from 1.21 eV and 1.56 eV to 0.94 eV and 1.66 eV, respectively. This indicates that the intermolecular C–F···H–C hydrogen bonding can perturb the electronic structures of the molecules. The change of the molecular electronic states is further confirmed by the STS measurements. Fig. 11b shows a high-resolution STM image of the CuPc-F₁₆CuPc binary structure with an intermolecular ratio of 2 : 1. The brighter molecules are attributed to the F₁₆CuPc molecule. The STS measured on the lobe of CuPc and F₁₆CuPc molecules in this binary structure and their single-component monolayers are shown in Fig. 11c. Similarly, as compared with the single-component monolayer, the HOMO peaks of CuPc and F₁₆CuPc shift to lower and higher binding energy, respectively. The degree of HOMO level shift differing from the UPS results may originate from the different supramolecular arrangements in this 2 : 1 system compared with their 1 : 1 mixture. The charge transfer behaviors in both the single-component monolayers and the binary donor–

acceptor blends are also calculated to reveal more insight into the intermolecular and molecule–substrate interactions. As shown in Fig. 11d, the amounts of electron transfer from graphene to pure CuPc and F₁₆CuPc monolayers are 0.04e and 0.22e, respectively. For the binary system, the electron transfer between CuPc and graphene is changed from receiving 0.04e to losing 0.01e. The electron transfer from graphene to F₁₆CuPc is increased to 0.29e. These changes originate from the weak intermolecular interactions in this binary system. The energy level shift in this weakly interacting binary molecular system can be explained using the gap states model. As the charge flow direction is opposite for CuPc in the pure monolayer and in the binary system, the Fermi level shifts from the bottom of the unoccupied gap states to the top of the occupied gap states. Hence, a large HOMO shift is observed for the CuPc molecule. For the F₁₆CuPc, the charge flow direction is the same for the single-component and binary systems, with only a small variation of the charge transfer amount. As the Fermi level is pinned to the gap states near the LUMO edge, the integration of a small range of unoccupied gap states below LUMO is sufficient to accommodate the further transferred electrons from HOPG to F₁₆CuPc. Therefore, only a small HOMO shift is observed for the F₁₆CuPc molecule. This

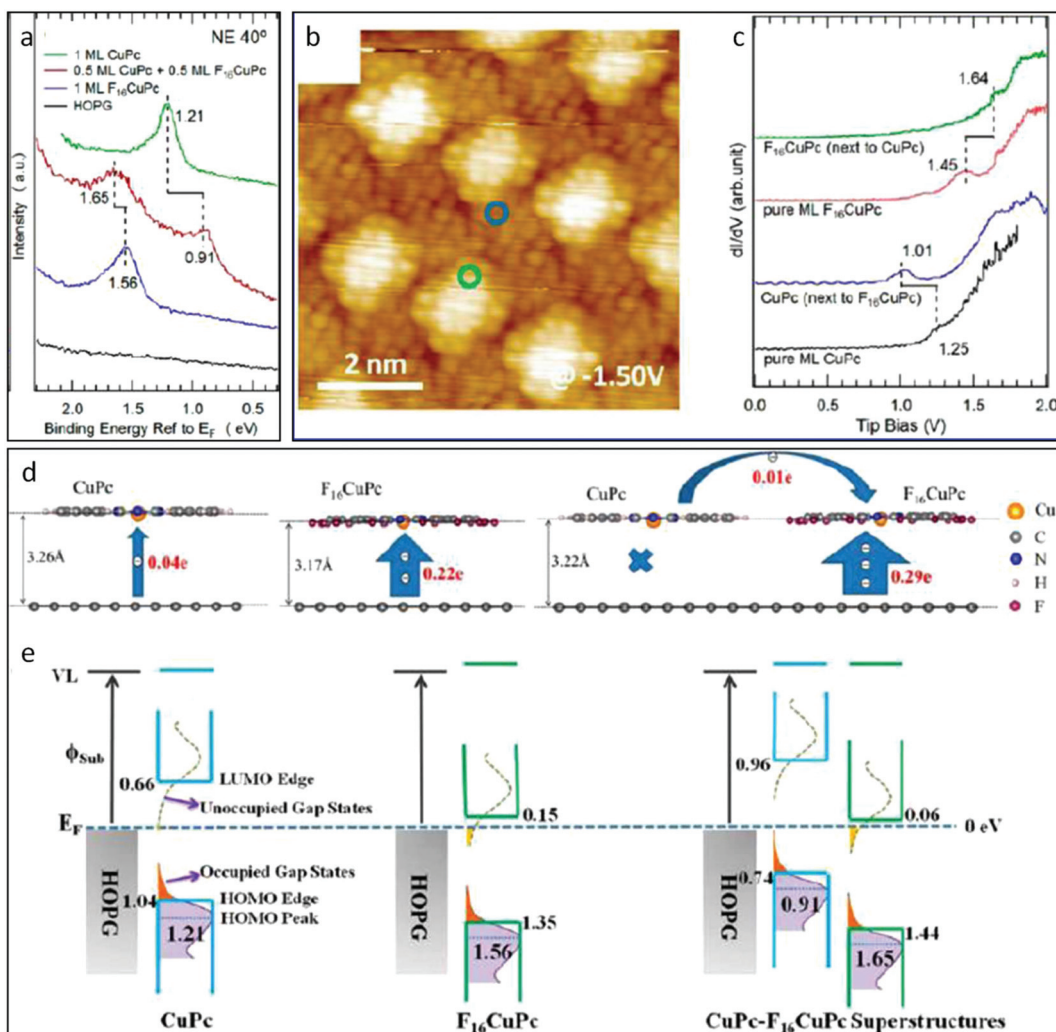


Fig. 11 (a) Valence band spectra at the low binding energy part for a CuPc and F₁₆CuPc monolayer and their 1:1 mixture on a HOPG substrate. The photoelectron takeoff angles relative to the analyzer are indicated in the figures. (b) Supramolecular packing structure of a CuPc-F₁₆CuPc binary network with an intermixing ratio of 2:1 ($V_{\text{tip}} = -1.50$ V, $8 \times 8 \text{ nm}^2$, $T = 77$ K; here the dark and bright features refer to the CuPc and F₁₆CuPc molecules, respectively). (c) STS spectra taken at the lobe of F₁₆CuPc molecules and CuPc molecules for both pure and mixed layers. (d) The calculated electron transfer between CuPc and HOPG, F₁₆CuPc and HOPG, as well as the transfer of electrons in their 1:1 mixture. (e) Schematic illustrations of gap-state-mediated weak interface charge transfer behaviours in explaining the significant energy level shift in weakly interacting binary molecular systems. The unoccupied and occupied gap states are indicated by the purple arrows in the figure, which are extended from the LUMO and HOMO edges, respectively, and decayed exponentially into the band gap. Reprinted from ref. 89, with permission from American Chemical Society, copyright 2014.

system clearly demonstrates that the electronic structures of the donor–acceptor nanostructures can be effectively modulated by the weak intermolecular interactions.

5.2 Charge transfer and energy level alignment in donor–acceptor heterojunctions

We have discussed the influence of intermolecular interactions on the electronic structures of the molecules in monolayer donor–acceptor blends. For practical applications in organic electronic devices, they usually contain multilayer stacked donor–acceptor heterojunctions or bulk donor–acceptor blends. Hence, a comprehensive understanding of the charge

transfer and energy level alignment at the donor–acceptor heterojunction interface is highly desired.

5.2.1 Intrinsic C₆₀/6T donor–acceptor heterojunction. By using the case study of C₆₀/6T,⁶² we discuss how the interactions in the C₆₀/6T determine the nanostructure formation and how the energy level is aligned at the interfaces. Fig. 12a–12e show the *in situ* synchrotron-based thickness-dependent PES measurements carried out to investigate this material system. PES measurements were performed after each sequential deposition of 6T or C₆₀ during the establishment of the heterojunction of C₆₀ on 6T on HOPG. In Fig. 12a, a small shift of the secondary electron cutoff (SECO) of 0.08 ± 0.02 eV when depositing C₆₀ on 6T from 0.3 nm to 6.0 nm is observed,

indicating that the vacuum level (VL) is nearly unchanged. This suggests that the degree of charge transfer at the $C_{60}/6T$ interface is very small and the interface is dominated by the $\pi-\pi$ interaction (mainly van der Waals forces) and the weak charge transfer interactions. The UPS spectra at the low binding energy part near the Fermi level are shown in Fig. 12b and 12c to reveal the evolution of the HOMOs during the formation of the $C_{60}/6T$ heterojunction interface. The typical HOMO related structure of 6T with the peak centered at 1.53 ± 0.02 eV is observed. Sequential deposition of C_{60} leads to the appearance of the HOMO peak related to C_{60} at 2.37 ± 0.02 eV. The valence band of the C_{60} is dominated by C_{60} -related features when C_{60} becomes 3.0 nm thick. Clearly, there is no apparent binding energy shift of both the 6T- and C_{60} -related structures during the deposition of C_{60} . This further confirms

the weak charge transfer between 6T and C_{60} . Fig. 12d and 12e show the core level measurements for the evolution of C 1s and S 2p during the deposition process, respectively. The C 1s spectrum for 1 nm 6T on HOPG (spectrum (2) in Fig. 12d) is dominated by the C(C) component at 284.4 ± 0.02 eV. After depositing 3 nm C_{60} , the C_{60} -related component at 285.1 ± 0.02 eV has dominated the C 1s spectrum (spectrum (6) in Fig. 12d). Also, during the C_{60} deposition process, no apparent shift of the C(C) component of both the 6T film and the C_{60} film is observed. A similar trend can be observed for S 2p spectra that the binding energy of both the 6T-related S $2p_{3/2}$ (164.2 ± 0.02 eV) and $2p_{1/2}$ (165.4 ± 0.02 eV) peaks remains constant during the deposition of C_{60} . Thus the core level spectra further confirm the weak interaction between C_{60} and 6T. Fig. 12f shows the schematic energy level alignment of $C_{60}/$

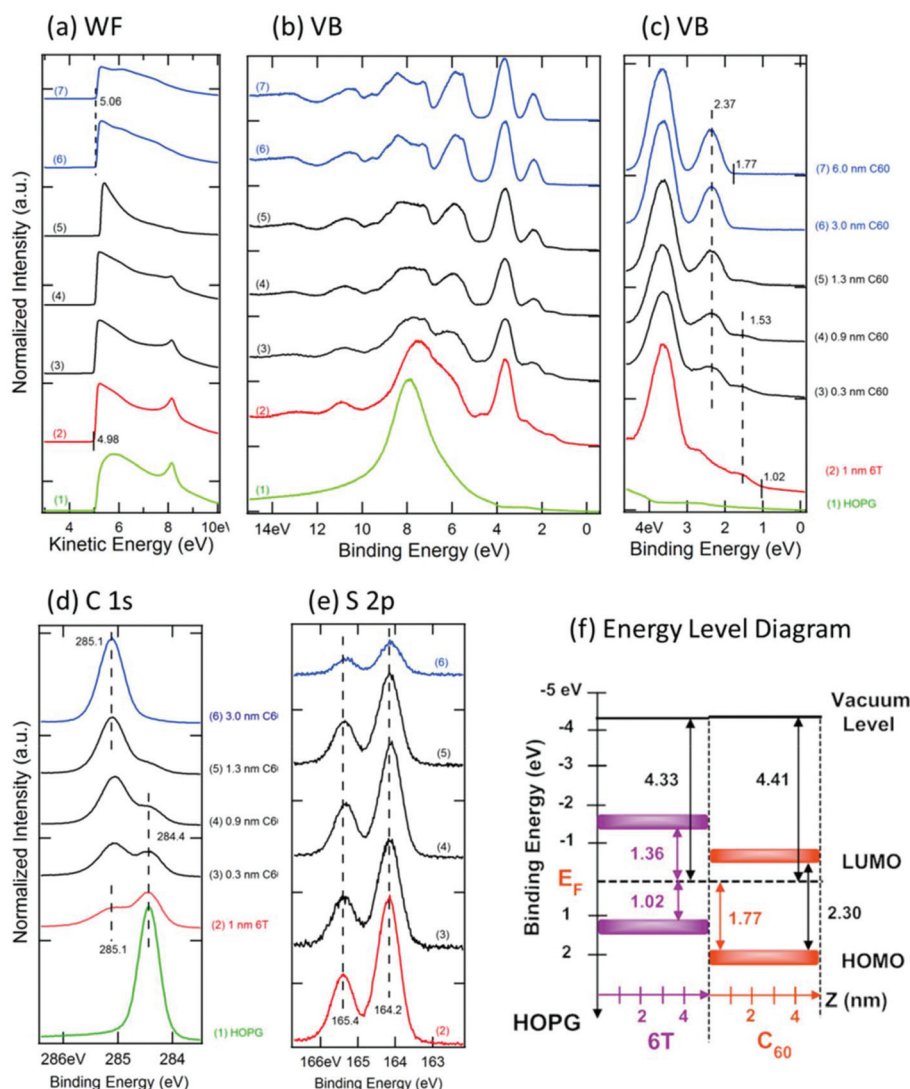


Fig. 12 Thickness dependent synchrotron PES spectra during the sequential deposition of C_{60} on 1 nm 6T covered HOPG at (a) the low kinetic energy region (secondary electron cutoff) and (b) the low binding energy region (the valance band region). (c) The corresponding valance band region near the Fermi level, and (d) C 1s and (e) S 2p core level spectra. (a)–(c) were measured with a photon energy of 60 eV, and (d) and (e) were measured with a photon energy of 350 eV. All binding energies are referenced to the substrate Fermi level. (f) Schematic energy level diagram at $C_{60}/6T/\text{HOPG}$ interfaces. (a–f) Reprinted from ref. 62, with permission from American Institute of Physics, copyright 2011.

6T on HOPG. The HOMO positions are derived from the UPS measurements. The transport band gap (HOMO–LUMO gap) and hence the LUMO positions are taken from previously reported inverse photoemission spectroscopy (IPES) measurements. As shown in Fig. 12f, there is a large energy barrier (~ 1.55 eV) between the HOMO of 6T and the LUMO of C_{60} , preventing apparent interfacial charge transfer. This is in good agreement with the observation of a nearly vacuum level alignment. However, such weak interactions can still induce the structural rearrangement of the underlying 6T nanostripe and the coexistence of three energetically stable structural motifs with well-defined supramolecular arrangements, including a C_{60} zigzag filament, a C_{60} hexagon and a C_{60} -pair filament, as shown in Fig. 4.³⁸

The large energy barrier (~ 1.55 eV) between the HOMO of 6T and the LUMO of C_{60} and the negligible charge transfer in the ground state is favourable for their applications in organic solar cells,^{8,95,96} as the V_{oc} is ultimately limited by this energy level offset. When the donor is optically excited, the electron in the LUMO will lower its energy by transfer to the LUMO of the acceptor. Under the influence of the built-in electric field caused by the asymmetric contacts, selective separation of the opposite charges takes place, with the holes being transported into the donor and electrons in the acceptor. In this way, the dissociation of excitons can efficiently occur at the donor–acceptor heterojunction.

5.2.2 Accumulation-type donor–acceptor heterojunction:

CuPc/ $F_{16}\text{CuPc}$. In some cases, significant charge transfer can happen at the donor–acceptor heterojunction interfaces, involving electron transfer from the donor layer to the acceptor layer. This type of heterojunction can be classified as an accumulation-type donor–acceptor heterojunction. Here, we use the example of the donor–acceptor heterojunction formed by CuPc/ $F_{16}\text{CuPc}$ on SiO_2 to illustrate the interfacial energy level alignment mechanism.^{97,98} Fig. 13a displays a schematic drawing of the standing CuPc/ $F_{16}\text{CuPc}$ heterojunction on SiO_2 , where both CuPc and $F_{16}\text{CuPc}$ molecules adopt a standing up configuration with their molecular π -planes oriented nearly perpendicular to the substrate surface.⁹⁷ As shown by Fig. 13a, by simply assuming the vacuum level alignment at the interface, the HOMO of the standing CuPc nearly aligns with the LUMO of the standing $F_{16}\text{CuPc}$, which can lead to spontaneous electron transfer from the top CuPc layer to the underlying $F_{16}\text{CuPc}$ film. The detailed charge transfer process can be clearly demonstrated by the thickness dependent energy level alignment at the CuPc/ $F_{16}\text{CuPc}$ heterojunction interface.⁹⁸ Fig. 13b–13d show the UPS evolution spectra during the deposition of CuPc molecules on a 5 nm standing $F_{16}\text{CuPc}$ film on SiO_2 as a function of CuPc nominal thickness for the HOMO and VL regions. Two distant regions for the energy level alignment can be identified from the UPS spectra. In region I (for CuPc thickness below 2 nm), the Fermi level is pinned at the HOMO leading edge; in region II (for CuPc thickness above 2 nm), the Fermi level moves into the gap and a band-bending like behaviour is observed for both HOMO and VL (Fig. 13e). This thickness dependent energy level align-

ment can be explained by the defect induced gap state model (Fig. 13e).^{99–101} Clearly, the large work function reduction upon deposition of CuPc on $F_{16}\text{CuPc}$ by 1.3 eV reveals the significant electron transfer from CuPc to the underlying $F_{16}\text{CuPc}$ (Fig. 13d). This is further corroborated by the observed Fermi-level pinning and the band-bending like behaviours at the valence band region (Fig. 13b and c).

Such strong interface charge transfers result in an accumulation type donor–acceptor heterojunction, with an electron accumulation layer in the n-type $F_{16}\text{CuPc}$ film and a hole accumulation layer in the p-type CuPc. This facilitates efficient charge transport of both electrons and holes at the donor–acceptor interface, *i.e.*, electron transport in the acceptor-type $F_{16}\text{CuPc}$ layer and hole transport in the donor-type CuPc layer. This can account for their applications in ambipolar OFETs.^{23,102–105} The accumulation type donor–acceptor heterojunction can also be used as a charge generation layer (CGL) in tandem OLED devices.^{106,107} All of the individual electroluminescent (EL) units in a tandem OLED are connected in series *via* a CGL in between.^{108–110} The CGL functions as both an internal anode and a cathode to generate intrinsic charge carriers. Upon allocation of an external electric field, the generated electrons and holes can be oppositely transported into the adjacent EL units. High-performance tandem OLED can be realized with the application of the highly efficient CGLs.

These well-defined organic donor–acceptor nanostructure arrays and heterojunctions can serve as ideal model systems to evaluate various interface properties at the molecular scale, including interfacial intermolecular interactions, charge transfer, interface dipole formation, energy level alignment, and interface nanostructuring. They also provide an ideal platform to understand how the intermolecular and interfacial interactions modulate the molecular nanostructure formation. By the combination of different experimental approaches, it is possible to achieve a comprehensive understanding of the origin of these interface properties and their implications in various organic electronic and/or optoelectronic devices, as well as provide design rules for the construction of organic donor–acceptor nanostructured heterojunctions with a desired functionality.

6. Conclusion and outlook

In this article, we review the recent progress in constructing organic donor–acceptor nanostructure arrays by molecular self-assembly, with particular emphasis on the donor–acceptor systems facilitated by surface nanotemplates or multiple intermolecular interactions. By using several model systems and combining the results from different experimental techniques (STM, UPS/XPS), we finally arrive at a fully coherent and comprehensive picture of the self-assembly of donor–acceptor nanostructures, and energy level alignment at the interfaces. The interface nanostructuring and energy level alignment strongly affect the performance of organic electronic devices, such as the light absorption, exciton dissociation, charge

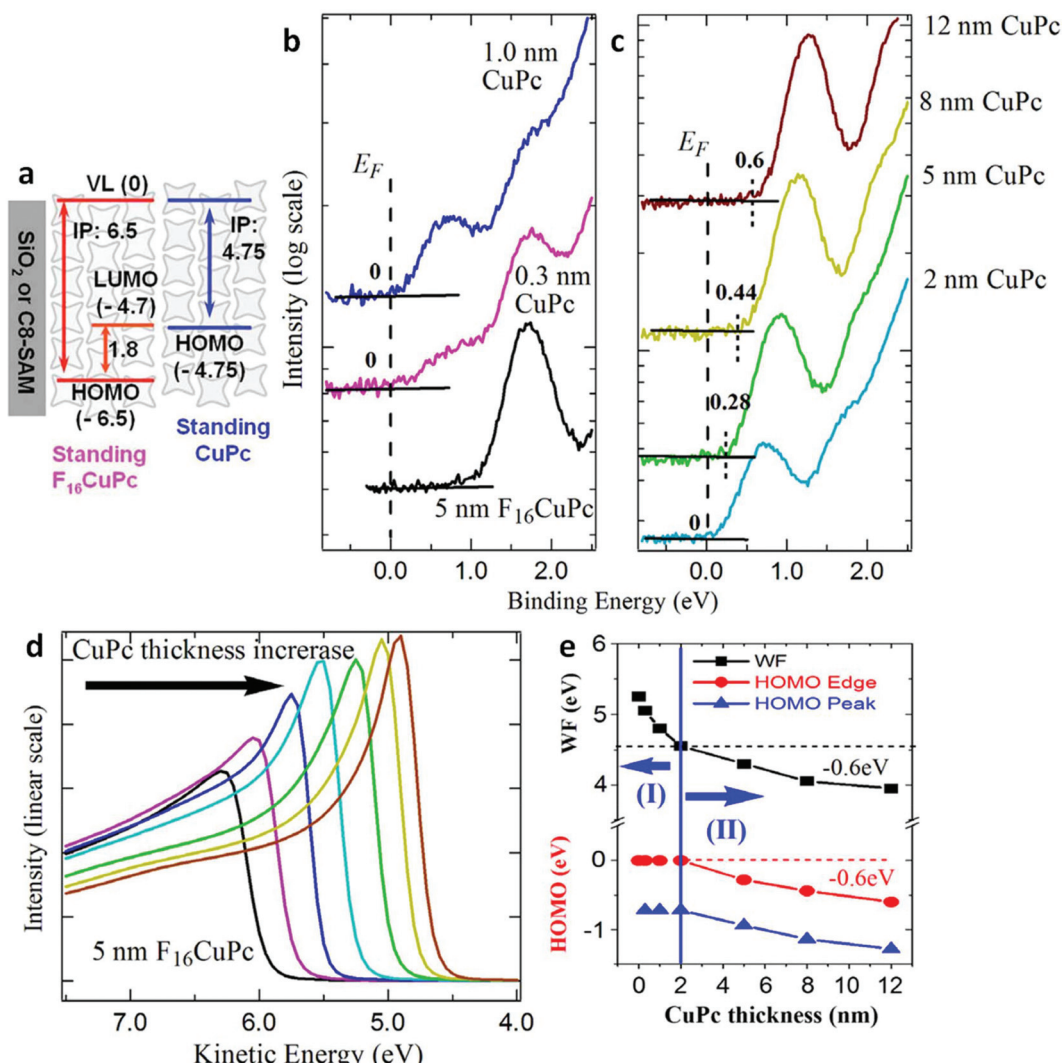


Fig. 13 Thickness dependent synchrotron PES spectra during the sequential deposition of CuPc on 5 nm F₁₆CuPc covered SiO₂. (a) Schematic drawing of the energy level alignment at the standing CuPc/F₁₆CuPc interface by assuming a vacuum level alignment. (b) and (c) The low binding energy part near the E_F region (the intensity is on a log scale) and (d) the low kinetic energy region (secondary electron cut-off and the intensity is on a linear scale) with a sample bias of -5 V. (e) Plot showing the change of the work function, CuPc HOMO edge and HOMO peak maximum as a function of CuPc thickness. All spectra were recorded with a photon energy of 60 eV. All binding energies are relative to the Fermi level position of the electron analyzer. (a) Reprinted from ref. 97, with permission from AIP Publishing LLC, copyright 2009. (b–e) Reprinted from ref. 98, with permission from Elsevier, copyright 2011.

transport and interfacial charge transfer. By carefully optimizing the interface properties, these nanostructured donor–acceptor systems are expected to play a key role in future development of organic electronic devices. In OPVs, these vertical, lateral and intermixed donor–acceptor nanojunctions can be used in the planar, bulk and mixed heterojunction solar cells. In FETs devices, the donor–acceptor heterojunction can serve as an efficient charge transport channel for electrons and holes respectively, leading to efficient ambipolar device operation.

Understanding the molecular self-assembly process of donor–acceptor systems and precise control of the resulting nanostructures are still in their early stages of development. Future research in this field will be directed towards the exten-

sion of organic donor–acceptor architectures to the third dimension. It is also necessary to correlate the structural properties with the electronic properties at the interface, which would eventually allow for a rational design of functional donor–acceptor nanostructures for future high-performance electronic and optoelectronic devices.

Acknowledgements

The authors acknowledge support from Singapore MOE grant R143-000-559-112, Singapore NRF-CRP grant R-143-001-608-281, National Key Basic Research Program of China

(2015CB856505), Jiangsu Province Government Research Platform Grant and NUSRI Seed Fund.

References

- 1 S. R. Forrest, *Nature*, 2004, **428**, 911–918.
- 2 D. Fyfe, *Nat. Photonics*, 2009, **3**, 453–455.
- 3 N. R. Armstrong, W. Wang, D. M. Alloway, D. Placencia, E. Ratcliff and M. Brumbach, *Macromol. Rapid Commun.*, 2009, **30**, 717–731.
- 4 Q. Zhang, B. Li, S. Huang, H. Nomura, H. Tanaka and C. Adachi, *Nat. Photonics*, 2014, **8**, 326–332.
- 5 H. Nakanotani, T. Higuchi, T. Furukawa, K. Masui, K. Morimoto, M. Numata, H. Tanaka, Y. Sagara, T. Yasuda and C. Adachi, *Nat. Commun.*, 2014, **5**, 4016.
- 6 Y. Sun, G. C. Welch, W. L. Leong, C. J. Takacs, G. C. Bazan and A. J. Heeger, *Nat. Mater.*, 2012, **11**, 44–48.
- 7 P. W. M. Blom, V. D. Mihailescu, L. J. A. Koster and D. E. Markov, *Adv. Mater.*, 2007, **19**, 1551–1566.
- 8 K. Cnops, B. P. Rand, D. Cheyns, B. Verreet, M. A. Empl and P. Heremans, *Nat. Commun.*, 2014, **5**, 3406.
- 9 S. M. Menke, W. A. Luhman and R. J. Holmes, *Nat. Mater.*, 2013, **12**, 152–157.
- 10 J. You, L. Dou, K. Yoshimura, T. Kato, K. Ohya, T. Moriarty, K. Emery, C.-C. Chen, J. Gao, G. Li and Y. Yang, *Nat. Commun.*, 2013, **4**, 1446.
- 11 J. R. Tumbleston, B. A. Collins, L. Yang, A. C. Stuart, E. Gann, W. Ma, W. You and H. Ade, *Nat. Photonics*, 2014, **8**, 385–391.
- 12 A. Tada, Y. Geng, Q. Wei, K. Hashimoto and K. Tajima, *Nat. Mater.*, 2011, **10**, 450–455.
- 13 Y. Wen and Y. Liu, *Adv. Mater.*, 2010, **22**, 1331–1345.
- 14 M. Muccini, *Nat. Mater.*, 2006, **5**, 605–613.
- 15 C. Wang, H. Dong, W. Hu, Y. Liu and D. Zhu, *Chem. Rev.*, 2011, **112**, 2208–2267.
- 16 O. Knopfmacher, M. L. Hammock, A. L. Appleton, G. Schwartz, J. Mei, T. Lei, J. Pei and Z. Bao, *Nat. Commun.*, 2014, **5**, 2954.
- 17 G. Lu, J. Blakesley, S. Himmelberger, P. Pingel, J. Frisch, I. Lieberwirth, I. Salzmann, M. Oehzelt, R. Di Pietro, A. Salleo, N. Koch and D. Neher, *Nat. Commun.*, 2013, **4**, 1588.
- 18 Y. Yang, R. C. da Costa, M. J. Fuchter and A. J. Campbell, *Nat. Photonics*, 2013, **7**, 634–638.
- 19 H. Ma, H.-L. Yip, F. Huang and A. K. Y. Jen, *Adv. Funct. Mater.*, 2010, **20**, 1371–1388.
- 20 Y. Kurosaka, S. Iwahashi, Y. Liang, K. Sakai, E. Miyai, W. Kunishi, D. Ohnishi and S. Noda, *Nat. Photonics*, 2010, **4**, 447–450.
- 21 A. P. Kulkarni, C. J. Tonzola, A. Babel and S. A. Jenekhe, *Chem. Mater.*, 2004, **16**, 4556–4573.
- 22 L.-M. Chen, Z. Xu, Z. Hong and Y. Yang, *J. Mater. Chem.*, 2010, **20**, 2575–2598.
- 23 J. Wang, H. Wang, X. Yan, H. Huang, D. Jin, J. Shi, Y. Tang and D. Yan, *Adv. Funct. Mater.*, 2006, **16**, 824–830.
- 24 M. Oehzelt, N. Koch and G. Heimel, *Nat. Commun.*, 2014, **5**, 4174.
- 25 F. Yang, M. Shtain and S. R. Forrest, *Nat. Mater.*, 2005, **4**, 37–41.
- 26 P. Peumans, S. Uchida and S. R. Forrest, *Nature*, 2003, **425**, 158–162.
- 27 S. R. Forrest, *MRS Bull.*, 2005, **30**, 28–32.
- 28 B. Bernardo, D. Cheyns, B. Verreet, R. D. Schaller, B. P. Rand and N. C. Giebink, *Nat. Commun.*, 2014, **5**, 3245.
- 29 C. J. Brabec, N. S. Sariciftci and J. C. Hummelen, *Adv. Funct. Mater.*, 2001, **11**, 15–26.
- 30 N. Koch, *J. Phys.: Condens. Matter*, 2008, **20**, 184008.
- 31 W. Chen, D.-C. Qi, H. Huang, X. Gao and A. T. S. Wee, *Adv. Funct. Mater.*, 2011, **21**, 410–424.
- 32 S. Zhong, J. Q. Zhong, H. Y. Mao, J. L. Zhang, J. D. Lin and W. Chen, *Phys. Chem. Chem. Phys.*, 2012, **14**, 14127–14141.
- 33 A. Llanes-Pallas, M. Matena, T. Jung, M. Prato, M. Stöhr and D. Bonifazi, *Angew. Chem., Int. Ed.*, 2008, **47**, 7726–7730.
- 34 J. A. Theobald, N. S. Oxtoby, M. A. Phillips, N. R. Champness and P. H. Beton, *Nature*, 2003, **424**, 1029–1031.
- 35 T. Huang, Z. Hu, A. Zhao, H. Wang, B. Wang, J. Yang and J. G. Hou, *J. Am. Chem. Soc.*, 2007, **129**, 3857–3862.
- 36 N. A. Wasio, R. C. Quardokus, R. P. Forrest, C. S. Lent, S. A. Corelli, J. A. Christie, K. W. Henderson and S. A. Kandel, *Nature*, 2014, **507**, 86–89.
- 37 T. Yokoyama, S. Yokoyama, T. Kamikado, Y. Okuno and S. Mashiko, *Nature*, 2001, **413**, 619–621.
- 38 M. E. Cañas-Ventura, W. Xiao, D. Wasserfallen, K. Müllen, H. Brune, J. V. Barth and R. Fasel, *Angew. Chem., Int. Ed.*, 2007, **46**, 1814–1818.
- 39 S. Stepanow, M. Lingenfelder, A. Dmitriev, H. Spillmann, E. Delvigne, N. Lin, X. Deng, C. Cai, J. V. Barth and K. Kern, *Nat. Mater.*, 2004, **3**, 229–233.
- 40 A. Dmitriev, H. Spillmann, N. Lin, J. V. Barth and K. Kern, *Angew. Chem., Int. Ed.*, 2003, **42**, 2670–2673.
- 41 K. Tahara, S. Furukawa, H. Uji-i, T. Uchino, T. Ichikawa, J. Zhang, W. Mamdouh, M. Sonoda, F. C. De Schryver, S. De Feyter and Y. Tobe, *J. Am. Chem. Soc.*, 2006, **128**, 16613–16625.
- 42 S. Lei, K. Tahara, F. C. De Schryver, M. Van der Auweraer, Y. Tobe and S. De Feyter, *Angew. Chem., Int. Ed.*, 2008, **47**, 2964–2968.
- 43 K. Wong, K.-Y. Kwon, B. V. Rao, A. Liu and L. Bartels, *J. Am. Chem. Soc.*, 2004, **126**, 7762–7763.
- 44 M. Böhringer, K. Morgenstern, W.-D. Schneider, M. Wühn, C. Wöll and R. Berndt, *Surf. Sci.*, 2000, **444**, 199–210.
- 45 Y. L. Huang, W. Chen, H. Li, J. Ma, J. Pflaum and A. T. S. Wee, *Small*, 2010, **6**, 70–75.
- 46 J. Adisoefoso, K. Tahara, S. Okuhata, S. Lei, Y. Tobe and S. De Feyter, *Angew. Chem., Int. Ed.*, 2009, **48**, 7353–7357.
- 47 M. Corso, W. Auwärter, M. Muntwiler, A. Tamai, T. Greber and J. Osterwalder, *Science*, 2004, **303**, 217–220.

- 48 H. L. Zhang, W. Chen, H. Huang, L. Chen and A. T. S. Wee, *J. Am. Chem. Soc.*, 2008, **130**, 2720–2721.
- 49 H. L. Zhang, W. Chen, L. Chen, H. Huang, X. S. Wang, J. Yuhara and A. T. S. Wee, *Small*, 2007, **3**, 2015–2018.
- 50 L. Chen, W. Chen, H. Huang, H. L. Zhang, J. Yuhara and A. T. S. Wee, *Adv. Mater.*, 2008, **20**, 484–488.
- 51 W. Chen, H. L. Zhang, H. Huang, L. Chen and A. T. S. Wee, *Appl. Phys. Lett.*, 2008, **92**, 193301.
- 52 J. L. Zhang, T. C. Niu, A. T. S. Wee and W. Chen, *Phys. Chem. Chem. Phys.*, 2013, **15**, 12414–12427.
- 53 T. Frederiksen, K. J. Franke, A. Arnau, G. Schulze, J. I. Pascual and N. Lorente, *Phys. Rev. B: Condens. Matter*, 2008, **78**, 233401.
- 54 W. Xiao, D. Passerone, P. Ruffieux, K. Aït-Mansour, O. Gröning, E. Tosatti, J. S. Siegel and R. Fasel, *J. Am. Chem. Soc.*, 2008, **130**, 4767–4771.
- 55 M. O. Blunt, J. C. Russell, N. R. Champness and P. H. Beton, *Chem. Commun.*, 2010, **46**, 7157–7159.
- 56 W. Jin, D. B. Dougherty, W. G. Cullen, S. Robey and J. E. Reutt-Robey, *Langmuir*, 2009, **25**, 9857–9862.
- 57 L. Piot, F. Silly, L. Tortech, Y. Nicolas, P. Blanchard, J. Roncali and D. Fichou, *J. Am. Chem. Soc.*, 2009, **131**, 12864–12865.
- 58 G.-B. Pan, X.-H. Cheng, S. Höger and W. Freyland, *J. Am. Chem. Soc.*, 2006, **128**, 4218–4219.
- 59 E. Mena-Osteritz and P. Bäuerle, *Adv. Mater.*, 2006, **18**, 447–451.
- 60 J.-R. Gong, H.-J. Yan, Q.-H. Yuan, L.-P. Xu, Z.-S. Bo and L.-J. Wan, *J. Am. Chem. Soc.*, 2006, **128**, 12384–12385.
- 61 H. Huang, W. Chen, L. Chen, H. L. Zhang, X. S. Wang, S. N. Bao and A. T. S. Wee, *Appl. Phys. Lett.*, 2008, **92**, 023105.
- 62 R. Wang, H. Y. Mao, H. Huang, D. C. Qi and W. Chen, *J. Appl. Phys.*, 2011, **109**, 084307.
- 63 J. Q. Zhong, H. Huang, H. Y. Mao, R. Wang, S. Zhong and W. Chen, *J. Chem. Phys.*, 2011, **134**, 154706.
- 64 L. M. A. Perdigão, E. W. Perkins, J. Ma, P. A. Staniec, B. L. Rogers, N. R. Champness and P. H. Beton, *J. Phys. Chem. B*, 2006, **110**, 12539–12542.
- 65 A. Ciesielski, M. El Garah, S. Haar, P. Kovaříček, J.-M. Lehn and P. Samorì, *Nat. Chem.*, 2014, **6**, 1017–1023.
- 66 L. Grill, M. Dyer, L. Lafferentz, M. Persson, M. V. Peters and S. Hecht, *Nat. Nanotechnol.*, 2007, **2**, 687–691.
- 67 K. W. Hipps, L. Scudiero, D. E. Barlow and M. P. Cooke, *J. Am. Chem. Soc.*, 2002, **124**, 2126–2127.
- 68 C. Bobisch, T. Wagner, A. Bannani and R. Möller, *J. Chem. Phys.*, 2003, **119**, 9804–9808.
- 69 T. N. Krauss, E. Barrena, H. Dosch and Y. Wakayama, *ChemPhysChem*, 2009, **10**, 2445–2448.
- 70 Y. Wakayama, D. G. de Oteyza, J. M. Garcia-Lastra and D. J. Mowbray, *ACS Nano*, 2011, **5**, 581–589.
- 71 A. Kahn, N. Koch and W. Gao, *J. Polym. Sci., Part B: Polym. Phys.*, 2003, **41**, 2529–2548.
- 72 N. Gonzalez-Lakunza, I. Fernández-Torrente, K. J. Franke, N. Lorente, A. Arnau and J. I. Pascual, *Phys. Rev. Lett.*, 2008, **100**, 156805.
- 73 T. R. Umbach, I. Fernandez-Torrente, J. N. Ladenthin, J. I. Pascual and K. J. Franke, *J. Phys.: Condens. Matter*, 2012, **24**, 354003.
- 74 I. Fernandez-Torrente, S. Monturet, K. J. Franke, J. Fraxedas, N. Lorente and J. I. Pascual, *Phys. Rev. Lett.*, 2007, **99**, 176103.
- 75 I. Fernández-Torrente, K. J. Franke and J. I. Pascual, *Phys. Rev. Lett.*, 2008, **101**, 217203.
- 76 A. Aviram and M. A. Ratner, *Chem. Phys. Lett.*, 1974, **29**, 277–283.
- 77 N. J. Tao, *Nat. Nanotechnol.*, 2006, **1**, 173–181.
- 78 R. M. Metzger, *Chem. Rev.*, 2003, **103**, 3803–3834.
- 79 A. S. Martin, J. R. Sambles and G. J. Ashwell, *Phys. Rev. Lett.*, 1993, **70**, 218–221.
- 80 M.-K. Ng and L. Yu, *Angew. Chem., Int. Ed.*, 2002, **41**, 3598–3601.
- 81 P. Jiang, G. M. Morales, W. You and L. Yu, *Angew. Chem., Int. Ed.*, 2004, **43**, 4471–4475.
- 82 R. H. M. Smit, Y. Noat, C. Untiedt, N. D. Lang, M. C. van Hemert and J. M. van Ruitenbeek, *Nature*, 2002, **419**, 906–909.
- 83 M. Elbing, R. Ochs, M. Koentopp, M. Fischer, C. von Hänsch, F. Weigend, F. Evers, H. B. Weber and M. Mayor, *Proc. Natl. Acad. Sci. U. S. A.*, 2005, **102**, 8815–8820.
- 84 M. L. Chabinyc, X. Chen, R. E. Holmlin, H. Jacobs, H. Skulason, C. D. Frisbie, V. Mujica, M. A. Ratner, M. A. Rampi and G. M. Whitesides, *J. Am. Chem. Soc.*, 2002, **124**, 11730–11736.
- 85 G. J. Ashwell, W. D. Tyrrell and A. J. Whittam, *J. Am. Chem. Soc.*, 2004, **126**, 7102–7110.
- 86 B. Mukherjee, K. Mohanta and A. J. Pal, *Chem. Mater.*, 2006, **18**, 3302–3307.
- 87 K. Mohanta and A. J. Pal, *Org. Electron.*, 2009, **10**, 960–964.
- 88 A. Bera and A. J. Pal, *Nanoscale*, 2013, **5**, 6518–6524.
- 89 J.-Q. Zhong, X. Qin, J.-L. Zhang, S. Kera, N. Ueno, A. T. S. Wee, J. Yang and W. Chen, *ACS Nano*, 2014, **8**, 1699–1707.
- 90 A. El-Sayed, P. Borghetti, E. Goiri, C. Rogero, L. Floreano, G. Lovat, D. J. Mowbray, J. L. Cabellos, Y. Wakayama, A. Rubio, J. E. Ortega and D. G. de Oteyza, *ACS Nano*, 2013, **7**, 6914–6920.
- 91 D. G. de Oteyza, J. M. García-Lastra, M. Corso, B. P. Doyle, L. Floreano, A. Morgante, Y. Wakayama, A. Rubio and J. E. Ortega, *Adv. Funct. Mater.*, 2009, **19**, 3567–3573.
- 92 A. El-Sayed, D. J. Mowbray, J. M. García-Lastra, C. Rogero, E. Goiri, P. Borghetti, A. Turak, B. P. Doyle, M. Dell'Angela, L. Floreano, Y. Wakayama, A. Rubio, J. E. Ortega and D. G. de Oteyza, *J. Phys. Chem. C*, 2012, **116**, 4780–4785.
- 93 J. L. Cabellos, D. J. Mowbray, E. Goiri, A. El-Sayed, L. Floreano, D. G. de Oteyza, C. Rogero, J. E. Ortega and A. Rubio, *J. Phys. Chem. C*, 2012, **116**, 17991–18001.
- 94 D. G. de Oteyza, I. Silanes, M. Ruiz-Osés, E. Barrena, B. P. Doyle, A. Arnau, H. Dosch, Y. Wakayama and J. E. Ortega, *Adv. Funct. Mater.*, 2009, **19**, 259–264.

- 95 M. Radziwon, A. L. F. Cauduro, M. Madsen and H.-G. Rubahn, *J. Nanomater.*, 2014, **2014**, 482372.
- 96 S. C. Veenstra, G. G. Malliaras, H. J. Brouwer, F. J. Esselink, V. V. Krasnikov, P. F. van Hutten, J. Wildeman, H. T. Jonkman, G. A. Sawatzky and G. Hadzioannou, *Synth. Met.*, 1997, **84**, 971–972.
- 97 W. Chen, S. Chen, S. Chen, Y. L. Huang, H. Huang, D. C. Qi, X. Y. Gao, J. Ma and A. T. S. Wee, *J. Appl. Phys.*, 2009, **106**, 064910.
- 98 H. Y. Mao, F. Bussolotti, D.-C. Qi, R. Wang, S. Kera, N. Ueno, A. T. S. Wee and W. Chen, *Org. Electron.*, 2011, **12**, 534–540.
- 99 F. Bussolotti, S. Kera, K. Kudo, A. Kahn and N. Ueno, *Phys. Rev. Lett.*, 2013, **110**, 267602.
- 100 T. Sueyoshi, H. Fukagawa, M. Ono, S. Kera and N. Ueno, *Appl. Phys. Lett.*, 2009, **95**, 183303.
- 101 J. Q. Zhong, H. Y. Mao, R. Wang, D. C. Qi, L. Cao, Y. Z. Wang and W. Chen, *J. Phys. Chem. C*, 2011, **115**, 23922–23928.
- 102 K. M. Lau, J. X. Tang, H. Y. Sun, C. S. Lee, S. T. Lee and D. Yan, *Appl. Phys. Lett.*, 2006, **88**, 173513.
- 103 J. Wang, H. Wang, X. Yan, H. Huang and D. Yan, *Appl. Phys. Lett.*, 2005, **87**, 093507.
- 104 F. Zhu, H. Wang, D. Song, K. Lou and D. Yan, *Appl. Phys. Lett.*, 2008, **93**, 103308.
- 105 F. Zhu, J. Yang, D. Song, C. Li and D. Yan, *Appl. Phys. Lett.*, 2009, **94**, 143305.
- 106 Y. Chen and D. Ma, *J. Mater. Chem.*, 2012, **22**, 18718–18734.
- 107 S. L. Lai, M. Y. Chan, M. K. Fung, C. S. Lee and S. T. Lee, *J. Appl. Phys.*, 2007, **101**, 014509.
- 108 H. Kanno, R. J. Holmes, Y. Sun, S. Kena-Cohen and S. R. Forrest, *Adv. Mater.*, 2006, **18**, 339–342.
- 109 H. Zhang, Y. Dai, D. Ma and W. C. H. Choy, *Appl. Phys. Lett.*, 2008, **92**, 109907.
- 110 L. S. Liao, W. K. Slusarek, T. K. Hatwar, M. L. Ricks and D. L. Comfort, *Adv. Mater.*, 2008, **20**, 324–329.